

## Full Length Article

# Mesoporous Ce-Zr solid solutions supported Ni-based catalysts for low-temperature CO<sub>2</sub> methanation by tuning the reaction intermediates

Leilei Xu<sup>a,\*</sup>, Xueying Wen<sup>a</sup>, Mindong Chen<sup>a,\*</sup>, Chufei Lv<sup>a</sup>, Yan Cui<sup>a</sup>, Xianyun Wu<sup>a</sup>, Cai-e Wu<sup>b</sup>, Bo Yang<sup>a</sup>, Zhichao Miao<sup>c</sup>, Xun Hu<sup>d,\*</sup>

<sup>a</sup> Collaborative Innovation Center of the Atmospheric Environment and Equipment Technology, School of Environmental Science and Engineering, Nanjing University of Information Science & Technology, Jiangsu Key Laboratory of Atmospheric Environment Monitoring and Pollution Control, 210044 Nanjing, China

<sup>b</sup> College of Light Industry and Food Engineering, Nanjing Forestry University, Nanjing 210037, China

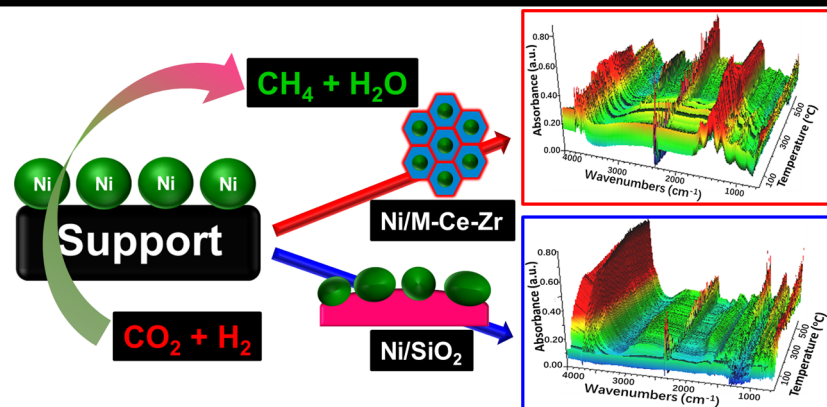
<sup>c</sup> School of Chemistry and Chemical Engineering, Shandong University of Technology, Zibo 255049, China

<sup>d</sup> School of Material Science and Engineering, University of Jinan, Jinan 250022, China



## GRAPHICAL ABSTRACT

## Reaction intermediates tuned by the catalytic supports



## ARTICLE INFO

## Keywords:

Mesoporous Ce-Zr solid solution  
Ni-based catalyst  
CO<sub>2</sub> methanation  
Low-temperature activity  
Reaction intermediates

## ABSTRACT

We facilely fabricated the mesoporous Ce-Zr solid solutions (Ce/Zr molar ratio = 0–100%) with excellent textural properties and employed them as the supports of the Ni-based catalysts for CO<sub>2</sub> methanation. These supported catalysts were systematically measured by various techniques, such as X-ray diffraction (XRD), N<sub>2</sub> physisorption, transmission electron microscope (TEM), selective area electron diffraction (SAED), X-ray photoelectron spectroscopy (XPS), H<sub>2</sub> temperature-programmed reduction (H<sub>2</sub>-TPR), CO<sub>2</sub> temperature-programmed desorption (CO<sub>2</sub>-TPD), etc. In this catalytic system, the influencing factors of the supports on the promotion of the low-temperature catalytic performances toward CO<sub>2</sub> methanation were carefully investigated. Besides, temperature-programmed surface reaction (TPSR) and *in-situ* diffused reflectance infrared Fourier transform spectroscopy (DRIFTS) of the CO<sub>2</sub> methanation were also carried out to investigate the reaction mechanism and the possible reaction intermediates. The kinetic study were also conducted to investigate the apparent activation energies of the CO<sub>2</sub> methanation over these Ni-based catalysts with different supports. The influencing factors on the stabilization of the metallic Ni active sites were also investigated by conducting the 40 h stability test over

\* Corresponding authors.

E-mail addresses: [leileixu88@gmail.com](mailto:leileixu88@gmail.com) (L. Xu), [chenmdnuist@163.com](mailto:chenmdnuist@163.com) (M. Chen), [Xun.Hu@outlook.com](mailto:Xun.Hu@outlook.com) (X. Hu).

<https://doi.org/10.1016/j.fuel.2020.118813>

Received 8 June 2020; Received in revised form 14 July 2020; Accepted 22 July 2020

0016-2361/© 2020 Elsevier Ltd. All rights reserved.

the 15Ni/M-Ce80Zr20 and 15Ni/SiO<sub>2</sub> catalysts. It was found that the Ni-based catalysts supported on the mesoporous Ce-Zr solid solutions were provided with advanced low-temperature activity owing to the redox property of the support, which could tune the reaction intermediates and decrease the apparent activation energy during the CO<sub>2</sub> methanation.

## 1. Introduction

With the prosperity of the worldwide economy, a large amount of CO<sub>2</sub> greenhouse gas has been emitted into the atmosphere owing to the consumption of the fossil fuels [1,2]. The CO<sub>2</sub> methanation to CH<sub>4</sub> is considered as one promising route for the effective CO<sub>2</sub> resource utilization of CO<sub>2</sub> because of the low reaction temperature [3–5]. Previous studies have demonstrated that the high catalytic activity and CH<sub>4</sub> selectivity could be achieved at the low reaction temperature [6,7]. However, it is difficult to accelerate the reaction rate at low reaction temperature because of the high kinetic barrier for the CO<sub>2</sub> activation. Specifically, the hydrogenation of the CO<sub>2</sub> to CH<sub>4</sub> should overcome a big kinetic barrier to obtain swift reaction rate and high selectivity [8]. Therefore, it is of great urgency to invent effective catalysts with promising low-temperature activities to overcome this difficulty.

Although the Ru [9,10], Rh [11,12], Pd [13,14], and other precious metal catalysts exhibit excellent low-temperature activity toward CO<sub>2</sub> methanation, they cannot be applicable for the industry because of the high price. Therefore, the Ni-based catalysts are extensively studied because of the low costs and excellent catalytic performances toward CO<sub>2</sub> methanation [4,15]. But the Ni-based catalysts often behave bad catalytic performances at low temperature. Besides, it is easy to cause the thermal sintering of the metallic active sites due to the exothermic feature of the CO<sub>2</sub> methanation [16,17], which would result in the rapid deactivation of the catalysts. The formation of gaseous carbonyl nickel (Ni(CO)<sub>4</sub>) is the main reason for thermal sintering at the low reaction temperature [18,19] and exothermic properties of the methanation of CO<sub>2</sub> would release heat and cause the formation of the hot spot [4,20]. Thus, developing highly efficient low-temperature Ni-based catalysts has become the important research topic in this field.

As for the supported catalyst, the support usually decides the structural properties of the catalyst. Furthermore, the characteristics of the support also critically affect the strong metal-support interaction, surface acidity or basicity, and electronic properties [21,22]. The oxides, such as SiO<sub>2</sub> [23], TiO<sub>2</sub> [24], Al<sub>2</sub>O<sub>3</sub> [25], ZrO<sub>2</sub> [26], and CeO<sub>2</sub> [27], have been widely employed as the supports. Among these oxides, the CeO<sub>2</sub> has unique redox property and high oxygen storage capacity because of the fast transition balance of Ce<sup>4+</sup>/Ce<sup>3+</sup> balance [28–30]. This would be very important to activate the CO<sub>2</sub> during the methanation process. However, the redox of CeO<sub>2</sub> support will be lost with the increase of the temperature because of the poor stability of pure CeO<sub>2</sub>. It has been reported that the incorporation of Zr atom into the CeO<sub>2</sub> lattice by isomorphous substitution could greatly stabilize the CeO<sub>2</sub> matrix [31,32]. Besides, the incorporation of ZrO<sub>2</sub> into the CeO<sub>2</sub> could induce serious deformation of the crystalline structures owing to the ionic radius difference between Ce<sup>4+</sup> (0.97 Å) and Zr<sup>4+</sup> (0.84 Å) cations, which would form the defects in the crystalline structure. Therefore, this could promote the CO<sub>2</sub> activation in CO<sub>2</sub> methanation. It was reported by Pan et al. that the bicarbonate, bidentate, and monodentate carbonate intermediates could be detected by *in-situ* DRIFTS analysis over the Ni/CeO<sub>2</sub>-ZrO<sub>2</sub> during the process of CO<sub>2</sub> methanation [33]. The bidentate species were considered as the main intermediates in the reaction. The oxygen storage capacity and redox property of the CeO<sub>2</sub>-ZrO<sub>2</sub> support greatly influenced the reaction intermediates by tuning the reaction pathway. It was reported by Ocampo et al. that the Ce/Zr molar ratio greatly influenced the performance of the Ni/CeO<sub>2</sub>-ZrO<sub>2</sub> catalyst and the CO<sub>2</sub> conversion over Ni/CZ (60–40) was the highest because the incorporation of ZrO<sub>2</sub> increases the oxygen mobility and promotes the formation of vacancies [34]. It was reported by

Iglesias et al. that the oxygen vacancy rate and utilization rate over the Ni/CeO<sub>2</sub>-ZrO<sub>2</sub> catalyst were higher than those over the Ni/CeO<sub>2</sub> catalyst [35]. They believed that the promoting effect of the incorporated Zr on the catalytic properties could be ascribed to higher oxygen mobility.

With the development of the material science, lots of novel supports, such as mesoporous materials [36–38], zeolites [39], carbon nanotube [40], grapheme [41], and MOFs [42,43], are commonly employed as the Ni-based catalyst supports due to their outstanding structural properties. Among these, mesoporous materials have been considered as promising catalytic supports, which could not only retain the metallic Ni active site in nano size range via confinement effect but also provide the reactants with more accessible metallic Ni active sites. Furthermore, their outstanding structural properties will be conducive to the mass transference during the reaction. Xu et al. reported that the ordered mesoporous Ni-Al composite catalysts with excellent structural property performed high CO<sub>2</sub> methanation catalytic activity because of the uniform and high dispersion of metallic Ni active sites [37,38]. Aziz et al. found that the abundant surface basic sites over the surface of Ni/MSN could enhance the CO<sub>2</sub> chemisorption and the reaction rate [44,45].

With the aim of constructing high performance Ni-based catalysts with advanced performances toward CO<sub>2</sub> methanation at low temperature, we prepared the Ni-based catalysts supported on the mesoporous Ce-Zr solid solutions were prepared and investigated their catalytic performance toward CO<sub>2</sub> methanation. We extensively investigated the effect of the Ce/Zr molar ratio of the supports on the enhancement of the low-temperature catalytic activity. Furthermore, we also found that the redox property of the support also played an significant role in the CO<sub>2</sub> activation according to the XPS and *in-situ* DRIFTS analyses. The TPSR and *in-situ* DRIFTS characterizations of the CO<sub>2</sub> methanation reaction process were carried out. Thus, the possible reaction intermediates and reaction routes could be concluded. Besides, the kinetic studies were also conducted over the Ni based Ce-Zr catalysts (Ce/Zr molar ratio = 0–100%) and SiO<sub>2</sub> supported reference catalyst. The influencing factors of the reaction apparent activation energy could be confirmed. The details about these studies were specifically described in the following text.

## 2. Experimental

### 2.1. Fabrication of the mesoporous ceria-zirconia solid solutions

The mesoporous Ce-Zr solid solutions (Ce<sub>x</sub>Zr<sub>1-x</sub>O<sub>2</sub>) with various Ce/Zr molar ratios (0–100%) were facily synthesized by the improved EISA strategy according to the literatures [32,46,47]. The detail of the specific synthesis procedure was described in the *S1-Supporting Information*. The obtained materials were denoted as M-CexZry, where x and y represented the Ce and Zr molar percentage ratios (x mol% = n<sub>Ce</sub>/(n<sub>Ce</sub> + n<sub>Zr</sub>) × 100% and y mol% = n<sub>Zr</sub>/(n<sub>Ce</sub> + n<sub>Zr</sub>) × 100%), respectively.

### 2.2. Preparation of the supported catalysts

The Ni-based catalysts supported on M-CexZry and the SiO<sub>2</sub> with 15.0 wt% metallic Ni loading amount were facily synthesized by the incipient wetness method. More details related to the preparation process were described in the *S2-Supporting Information*. The obtained catalysts with M-CexZry and the SiO<sub>2</sub> supports were abbreviated as 15Ni/M-CexZry and 15Ni/SiO<sub>2</sub>, respectively.

### 2.3. Characterizations of the supports and catalysts

The supports and catalysts were systematically characterized by various characterization techniques, such as X-ray powder diffraction (XRD),  $N_2$  physisorption, transmission electron microscopy (TEM), selected area electron diffraction (SAED), X-ray photoelectron spectroscopy (XPS),  $H_2$  temperature programmed reduction ( $H_2$ -TPR), and  $CO_2$  temperature programmed desorption ( $CO_2$ -TPD). Besides, the temperature programmed surface reaction (TPSR) and *in-situ* diffused reflectance infrared Fourier transform spectroscopy (DRIFTS) of  $CO_2$  methanation were carried to analyze the reaction intermediates according to the procedure reported elsewhere [48,49]. The specific procedures and equipment information of the characterization were summarized in S3-Supporting Information.

### 2.4. Evaluations of the catalytic performances

The evaluations of the catalytic activities, long-term stabilities, and kinetic studies of the catalysts toward  $CO_2$  methanation were carried out on a micro-atmospheric fixed-bed reactor, where the influence of the heat transference and/or mass transference could be minimized. Their specific operation procedures and calculation formulas were carefully stated in S4-Supporting Information.

## 3. Results and discussions

### 3.1. Characterizations of the M-CexZry supports

#### 3.1.1. XRD analysis

The XRD analysis was carried out to study the crystallinity of the M-CexZry supports. Fig. 1 displayed the XRD patterns of the M-CexZry supports (Ce/Zr molar ratio = 0–100%). As can be observed, the typical peaks of Ce-Zr solid solutions (e.g. JCPDS Card No. 38–1436,  $Ce_{0.5}Zr_{0.5}O_2$ ) with the fluorite structure appeared in these XRD patterns, which suffered some peak shift compared with the  $CeO_2$  (JCPDS Card No. 43–1002) and  $ZrO_2$  (JCPDS Card No. 34–0394) references. This could be ascribed to the difference between the radiuses of  $Ce^{4+}$  (0.97 Å) and  $Zr^{4+}$  (0.84 Å) cations [32,50]. When the isomorphous substitution of the smaller  $Zr^{4+}$  with larger  $Ce^{4+}$  took place, the interplanar spacing of the  $Ce_xZr_{1-x}O_2$  solid solution became bigger. Thus, it could be observed in Fig. 1 that the XRD diffraction peaks gradually shifted to lower  $2\theta$  values as the Ce/Zr molar ratio increased. Besides, it was noteworthy that the XRD peaks of the M-CexZry solid solution were wide, suggesting that these prepared supports were in the nanocrystalline state. There was no additional characteristic diffraction peaks of  $ZrO_2$  and  $CeO_2$  phases observed in the XRD pattern of M-CexZry solid solutions. This indicated that  $ZrO_2$  and  $CeO_2$  could infiltrate into each other's lattice to form the uniform solid solution.

#### 3.1.2. $N_2$ Physisorption analysis

These M-CexZry supports were characterized by  $N_2$  physisorption to investigate their textural properties. As exhibited in Fig. 2 (1), most of the investigated samples possessed IV H2 shaped isotherms. This suggested the presence of the mesoporous channels in “ink-bottle” shape based on the shape of isotherm. Furthermore, Fig. 2 (2) displayed the pore size distribution curves of this series of M-CexZry supports. We could observe that most of the supports possessed narrow pore size distributions in 4.0–8.0 nm range. Besides, the structural properties of the M-CexZry were summarized in Table 1. All the M-CexZry calcined at 500 °C possessed large  $S_{BET}$  up to 72.7  $m^2/g$ , big  $V_{BJH}$  up to 0.12  $cm^3/g$ , and APD in the range of mesopore (2.0–50.0 nm, IUPAC). Compared with the  $CeO_2$  (51.8  $m^2/g$ ) and  $ZrO_2$  (35.4  $m^2/g$ ) single supports, the Ce-Zr solid solution supports displayed a bit larger  $S_{BET}$ . This suggested that the formation of the solid solution could favor the improvement of the textural properties of the supports.

#### 3.1.3. TEM analysis

The transmission electronic microscopy (TEM) analyses of the M-CexZry solid solutions were conducted and their TEM images were shown in Fig. 3. It could be clearly observed in the Fig. 3 (a), (c), and (e) that all the samples possessed the worm-like mesoporous channels, which ought to be composed of the small  $Ce_xZr_{1-x}O_2$  solid solution nanoparticles. As for the formation of mesostructure in the M-CexZry solid solutions, it was supposed that the assembly of  $Ce^{3+}$  and  $Zr^{4+}$  cations around the P123 micelle with specific shapes (e.g. worm-like pore) was carried out. Thus, the small nanoparticles with worm-like mesoporous channels could be finally formed after the removal of the P123 template by calcination. Furthermore, the HRTEM analyses of these samples were also conducted to further investigate the crystalline details of the nanoparticles. As displayed in Fig. 3 (b), (d), and (f), the (111) crystal plane could be observed with the lattice spacing around 0.305 nm, suggesting the good crystallinity of these M-CexZry solid solution supports.

### 3.2. Characterizations of the as-prepared 15Ni/M-CexZry and 15Ni/SiO<sub>2</sub> catalysts

#### 3.2.1. XRD analysis

The XRD patterns of the 15Ni/M-CexZry and 15Ni/SiO<sub>2</sub> catalysts were exhibited in Fig. 4. Although the as-prepared 15Ni/M-CexZry catalysts had the same NiO loading amount, the intensities of the NiO characterization diffraction peaks (JCPDS Card No. 47-1049) of the as-prepared 15Ni/M-CexZry catalysts were a bit different. Generally, the intensities of the NiO diffraction peaks over the Ce-Zr solid solutions and  $CeO_2$  supported catalyst were much weaker than those with pure  $ZrO_2$  as support. This indicated that NiO species was more preferably dispersed on the Ce-Zr solid solutions and  $CeO_2$  supports. Specifically, the 15Ni/M-Ce40Zr60, 15Ni/M-Ce80Zr20, and 15Ni/M-Ce100 catalysts performed excellent dispersion of NiO. The main reason for this might be owing to the presence of  $Ce^{4+}$  species and they could promote the generation of oxygen vacancies and oxygen storage properties, which was helpful to promote the high dispersion of NiO. As for the positions of the diffraction peaks, the characteristic peaks of NiO did not undergo any drift; however, as the comparison, the diffraction peaks of the M-CexZry solid solution supports gradually migrated toward low  $2\theta$  value direction as the molar ratio of Ce/Zr increased. This was caused by the isomorphous substitution of the smaller  $Zr^{4+}$  (0.84 Å) with larger  $Ce^{4+}$  (0.97 Å) with different radiuses [32,50]. As a result, the interplanar spacing of the  $Ce_xZr_{1-x}O_2$  solid solution became bigger and the  $2\theta$  shifted to lower value. Furthermore, the XRD pattern

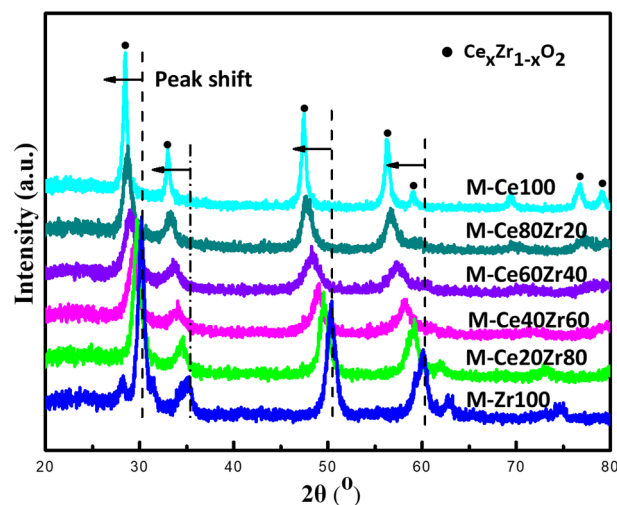


Fig. 1. X-ray diffraction patterns of mesoporous M-CexZry supports with different Ce/Zr ratios calcined at 500 °C.

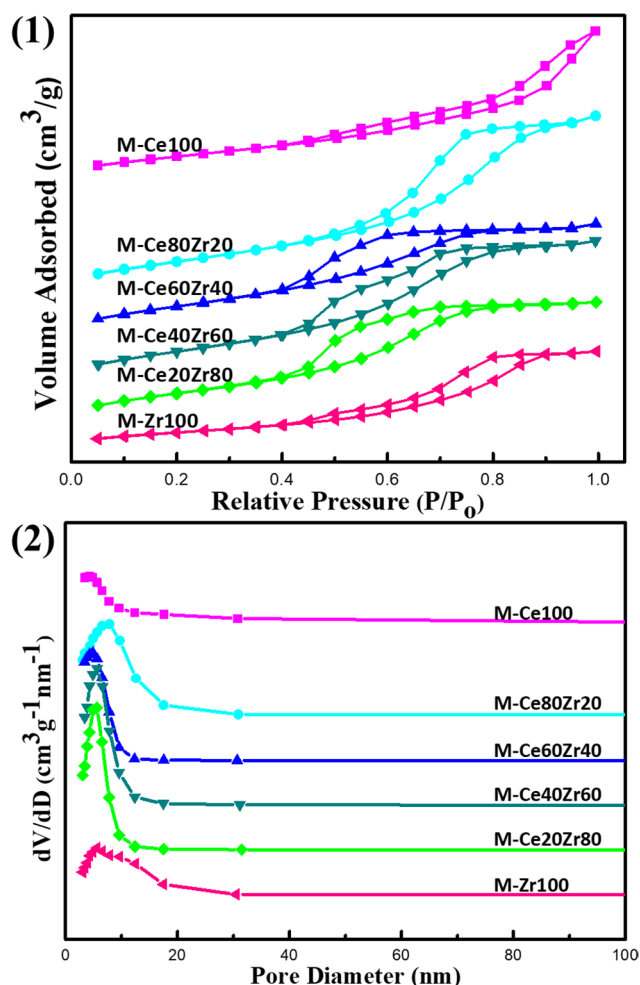


Fig. 2. (1)  $N_2$  adsorption-desorption isotherms and (2) pore size distribution curves of mesoporous M-CexZry supports.

Table 1

Structural properties of mesoporous M-CexZry supports and 15Ni/M-CexZry catalysts with different Ce/Zr ratios.

Samples	$S_{BET}^a$ ( $m^2/g$ )	$V_{BJH}^b$ ( $cm^3/g$ )	APD <sup>c</sup> (nm)	Type
M-Ce100	51.8	0.09	4.3	IV H2
M-Ce80Zr20	68.9	0.12	7.9	IV H2
M-Ce60Zr40	70.7	0.07	4.9	IV H2
M-Ce40Zr60	72.7	0.09	5.6	IV H2
M-Ce20Zr80	67.8	0.08	5.6	IV H2
M-Zr100	35.4	0.07	5.6	IV H2
15Ni/M-Ce100	6.68	0.10	61.8	IV H3
15Ni/M-Ce80Zr20	45.3	0.12	9.3	IV H2
15Ni/M-Ce60Zr40	45.8	0.08	6.4	IV H2
15Ni/M-Ce40Zr60	38.9	0.10	10.9	IV H2
15Ni/M-Ce20Zr80	38.9	0.10	10.5	IV H2
15Ni/M-Zr100	13.2	0.06	18.9	IV H3

<sup>a</sup>  $S_{BET}$  stands for the specific area calculated based on Brunauer-Emmett-Teller theory.

<sup>b</sup>  $V_{BJH}$  stands for the pore volume calculated based on Barrett-Joyner-Halenda theory.

<sup>c</sup> APD stands for the average pore diameter.

of 15Ni/SiO<sub>2</sub> reference catalyst with commercial SiO<sub>2</sub> support was also included in the Fig. 4. The 15Ni/SiO<sub>2</sub> catalyst displayed much higher NiO diffraction peak intensities than 15Ni/M-CexZry catalysts, although SiO<sub>2</sub> possessed much larger specific surface area (171.1  $m^2/g$ ) than M-CexZry supports. The reason for this might be attributed to the stronger metal-support interactions of 15Ni/M-CexZry catalysts than that of

15Ni/SiO<sub>2</sub> catalyst.

### 3.2.2. $N_2$ Physisorption analysis

Fig. 5 (1) displayed the isotherms of 15Ni/M-CexZry catalysts. It was found that the isotherms of these catalysts (IV H2) were identical to their corresponding M-CexZry supports. This indicated that the loading process and the subsequent calcination had slight effect on the porous structure of the catalyst. However, the hysteresis loops of 15Ni/M-Ce100 and 15 Ni/M-Zr100 were changed into H3 type, indicating that the ink-bottle shaped mesopores of M-Ce100 and M-Zr100 supports were partly blocked by the NiO nanoparticles because of their relatively small  $S_{BET}$  and  $V_{BJH}$ . Thus, their mesopores were of the wedge-shape after Ni loading. Besides, the PSD curves of the 15Ni/M-CexZry catalysts were shown in Fig. 5 (2). As can be observed, except for the 15Ni/M-Ce100 and 15Ni/M-Zr100 catalysts, the pore size distributions of the catalysts were relatively narrow centered on 10.0 nm and 28.5 nm, respectively. As comparison, the catalysts with M-Ce100 and M-Zr100 as the supports exhibited wide pore size distributions. Table 1 also summarized the structural properties of the 15Ni/M-CexZry catalysts. It could be seen in the table that the  $S_{BET}$  and  $V_{BJH}$  of the catalysts were lower than those of their supports. The reason for this was possibly ascribed to the blockage of the mesopores by the loaded NiO nanoparticles. The average pore diameters of catalysts was a bit higher than those of the corresponding supports. This suggested that the mesoporous framework successfully remained and the thermal shrinkage of the mesoporous framework had been successfully suppressed to some extent after the catalyst preparation and calcination, demonstrating the outstanding thermal stability.

### 3.2.3. TEM and SAED analyses

The TEM analyses of the 15Ni/M-CexZry were conducted. As shown in the Fig. 6, these Ni-based catalysts performed similar mesostructure to their corresponding supports with worm-like mesoporous channels in these investigated catalysts, suggesting the high dispersion of NiO nanoparticles. Besides, the selected area electron diffraction (SAED) were also carried out and their images were illustrated in the insets of the Fig. 6. Generally, the diffraction rings of the selected area were very clear dotted with some detracted dots of the array, indicating that the mesoporous wall was of high crystallinity.

### 3.2.4. XPS analysis

The XPS analysis was carried out to check the composition and coordination states of the surface elements of the catalysts. The XPS profiles of the 15Ni/M-CexZry with different Ce/Zr ratios were displayed in Fig. 7. As can be observed in the Fig. 7 (1), the main Ni 2p<sub>3/2</sub> and Ni 2p<sub>1/2</sub> peaks of the 15Ni/M-CexZry catalysts were located at 853.9 eV and 872.0 eV with similar intensities, respectively. It was of great interest to find that the Ni 2p<sub>3/2</sub> peaks of these samples were accompanied by the shoulder peaks centered at 855.5 eV. As well known, the free NiO possessed the Ni 2p<sub>3/2</sub> peak with the binding energy centered around 854.0 eV [51], which was equal to the binding energy value of the 15Ni/M-CexZry catalysts. This implied the presence of the NiO over the 15Ni/M-CexZry surface. Besides, the Ni 2p<sub>3/2</sub> shoulder peaks at 855.5 eV indicated that the nickel species also had a higher binding energy than the free NiO. The reason for this could be attributed to the formation of strong metal-support interaction between the NiO and the M-CexZry support. Besides, it was reported that the Ce-Zr solid solution support might be partially substituted by the surface Ni<sup>2+</sup>, which subsequently contributed to the facile reduction of the catalyst. For the Zr 3d spectra, it was found in Fig. 7 (2) that the Zr 3d<sub>5/2</sub> peaks of the catalysts were centered around 182.3 eV, which could be contributed to the Zr species in +4 oxidation state in the form of Zr<sup>4+</sup> according to previous reports [32,52]. It was also noteworthy that the decrease of Ce/Zr molar ratio caused the increase of the peak intensity of Zr 3d. This should be ascribed to the increasing concentration of the



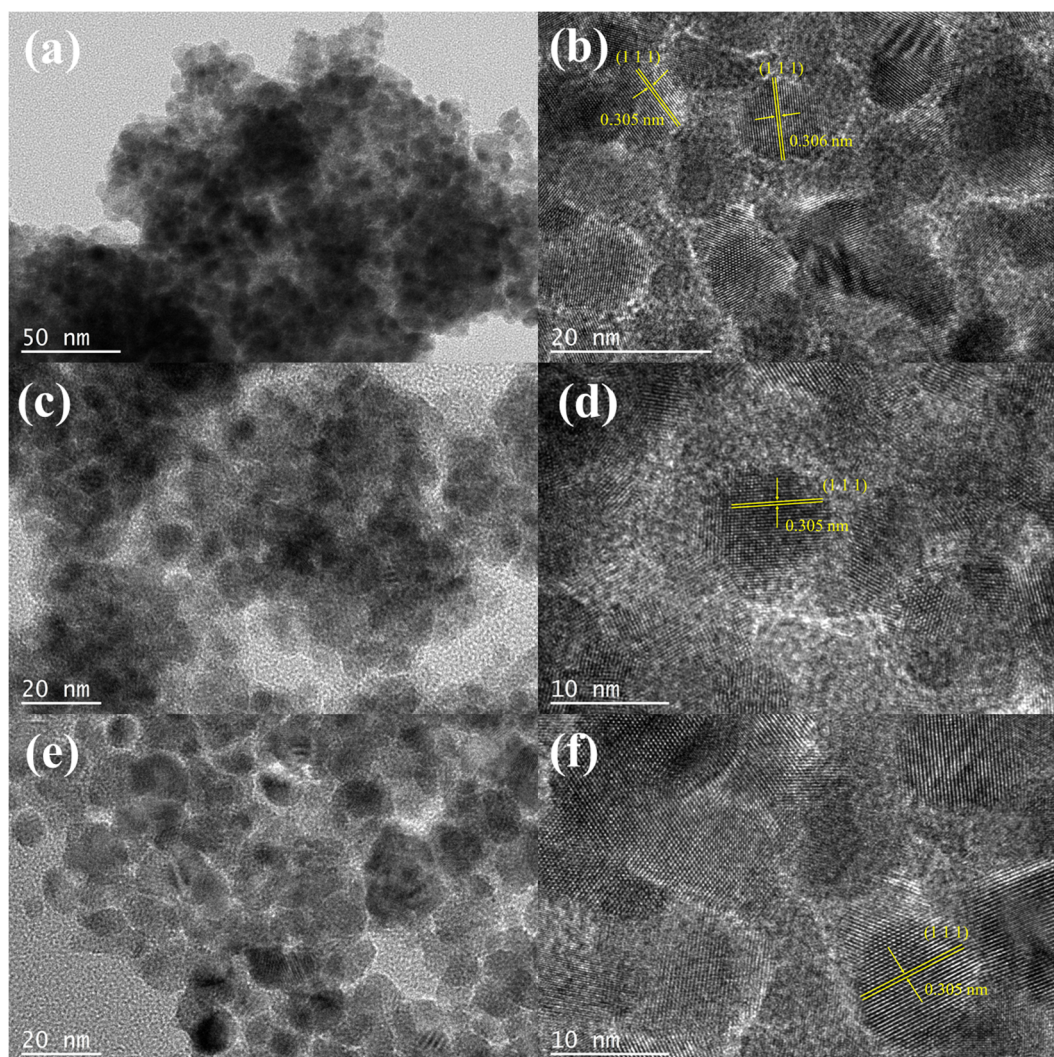


Fig. 3. Transmission electron microscope images of M-Ce<sub>x</sub>Zr<sub>1-x</sub> supports: (a) and (b) M-Ce<sub>50</sub>Zr<sub>50</sub>, (c) and (d) M-Ce<sub>60</sub>Zr<sub>40</sub>, (e) and (f) M-Ce<sub>80</sub>Zr<sub>20</sub>.

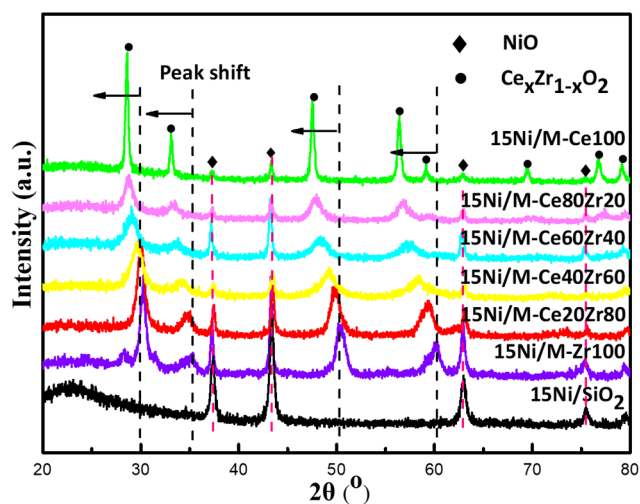


Fig. 4. X-ray diffraction patterns of 15Ni/M-Ce<sub>x</sub>Zr<sub>1-x</sub> catalysts.

surface Zr<sup>4+</sup>. As for the XPS profiles of Ce 3d, they were exhibited in the Fig. 7 (3). As could be observed, compared with the Ni 2p and Zr 3d spectra, the Ce 3d spectra were more complicated and composed of lots of individual overlapping peaks. The peak shapes of Ce 3d spectra of

15Ni/M-Ce<sub>x</sub>Zr<sub>1-x</sub> catalysts were similar and the peak intensities gradually increased with the increase of the Ce/Zr ratio. Generally, the profiles of Ce 3d could be divided into two sets of spin-orbit multiple peaks according to the classification of Burroughs et al. [53]. The specific division was listed as the following. Specifically, the peak positions of Ce<sup>3+</sup> were located at 885.3 eV (v') and 903.4 eV (u') and the peak positions of Ce<sup>4+</sup> were at 882.7 eV (v), 889.5 eV (v'), 898.7 eV (v''), 901.2 eV (u), 907.5 eV (u'), and 916.8 eV (u'') [54]. It could be confirmed that two types of Ce<sup>4+</sup> and Ce<sup>3+</sup> were coexisting over the surface of these catalysts, which could endow the catalysts with excellent redox properties. As regards the O 1s, it was found in Fig. 7 (4) that both the peak intensity and shape of profiles of these catalysts were great similar. Specifically, the O 1s displayed a main peak (529.3 eV) and a shoulder peak (531.0 eV) over all the samples. Specifically, the shoulder peak at 531.0 eV was attributable to the surface O<sup>2-</sup> anions, which was bonded with the Ce<sup>3+</sup>. In order to maintain the charge neutrality, the oxygen vacancy would be generated based on the previous reports [32,54].

The comparative XPS studies of the 15Ni/M-Ce<sub>80</sub>Zr<sub>20</sub> and 15Ni/SiO<sub>2</sub> catalysts were also carried out to investigate the effect of the support. As shown in Fig. 8 (1), the 15Ni/M-Ce<sub>80</sub>Zr<sub>20</sub> displayed a main Ni 2p<sub>3/2</sub> peak at 853.9 eV and a Ni 2p<sub>1/2</sub> peak at 872.0 eV, respectively. As a comparison, the 15Ni/SiO<sub>2</sub> only exhibited one Ni 2p<sub>3/2</sub> peak around 854.5 eV. This suggested that the coordinating and the electronic statuses of the surface NiO were greatly influenced by the type of

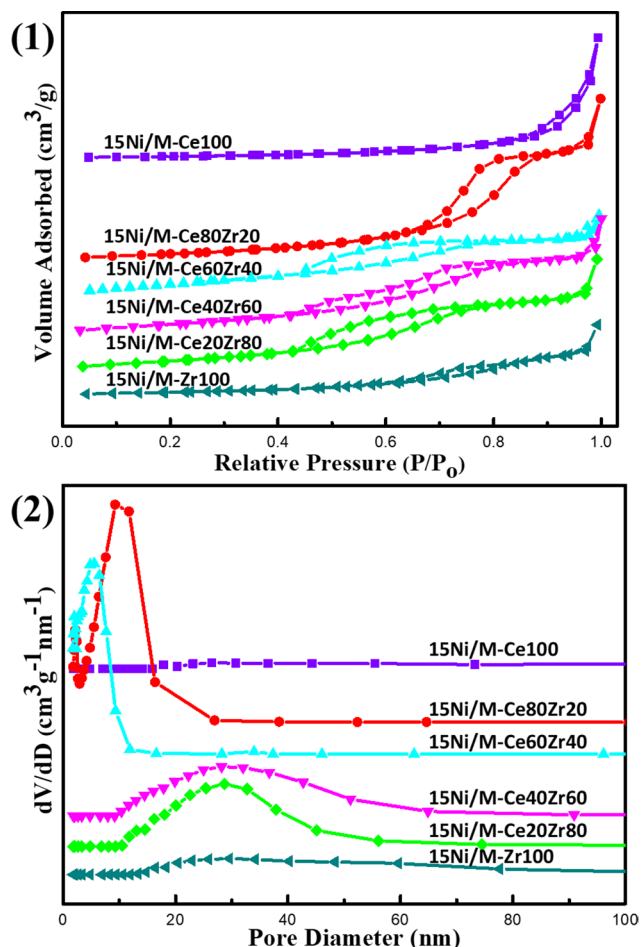


Fig. 5. (1) N<sub>2</sub> adsorption-desorption isotherms and (2) pore size distribution curves of 15Ni/M-CexZry catalysts.

the catalytic supports. As for the O 1s spectra of 15Ni/M-Ce80Zr20 and 15Ni/SiO<sub>2</sub> catalysts in Fig. 8 (2), it could be observed that their profile shapes were greatly different. Specifically, the 15Ni/M-Ce80Zr20 catalyst displayed an asymmetrical spectrum with a main O 1s peak around 529.3 eV and a shoulder peak near 531.0 eV; as a comparison, the 15Ni/SiO<sub>2</sub> catalyst almost displayed a symmetrical O 1s peak centered around 532.5 eV with a very tiny shoulder peak around 529.3 eV. The main reason for this could be originated from the different coordination environments of the oxygen species, which were greatly affected and decided by the feature of the supports. Specifically, the broad shoulder peak of the 15Ni/M-Ce80Zr20 catalyst could be ascribed to the O<sup>2-</sup> bonded to the trivalent Ce<sup>3+</sup> cations, which were generated as a result of oxygen vacancy formation to maintain charge neutrality. Thus, an additional O1s shoulder peak at relatively higher binding energy was ultimately formed. As for the 15Ni/SiO<sub>2</sub> catalyst, its symmetrical O1s peak suggested the absence of the oxygen vacancy in the SiO<sub>2</sub> support.

Besides, the specific values of the binding energies of the Ni, O, Ce, and Zr elements were also displayed in Table 2. The 15Ni/SiO<sub>2</sub> catalyst performed different Ni 2p<sub>3/2</sub> and O 1s binding energies with 15Ni/M-CexZry catalysts due to the support effect. Furthermore, the ratio of the O 1s shoulder peak area were summarized in Table 3. It could be observed that the 15Ni/M-CexZry catalysts displayed various O 1s shoulder peak area ratios from 37.2% to 58.0%, which were much higher than the 3.5% over 15Ni/SiO<sub>2</sub> catalyst. This suggested that the redox properties of the 15Ni/M-CexZry catalysts were much better than that of the 15Ni/SiO<sub>2</sub> reference catalyst because of the richer surface oxygen vacancies. Besides, the 15Ni/M-Ce80Zr20 catalyst possessed the highest O 1s shoulder peak area ratio (58.0%) among the 15Ni/M-CexZry catalysts because the concentration of the surface oxygen vacancy over the 15Ni/M-Ce80Zr20 catalyst was the highest. This would further influence the catalytic performance toward CO<sub>2</sub> methanation.

### 3.2.5. H<sub>2</sub>-TPR analysis

The H<sub>2</sub>-TPR was carried out to study the metal-support interaction over the 15Ni/M-CexZry and 15Ni/SiO<sub>2</sub> catalysts and their profiles

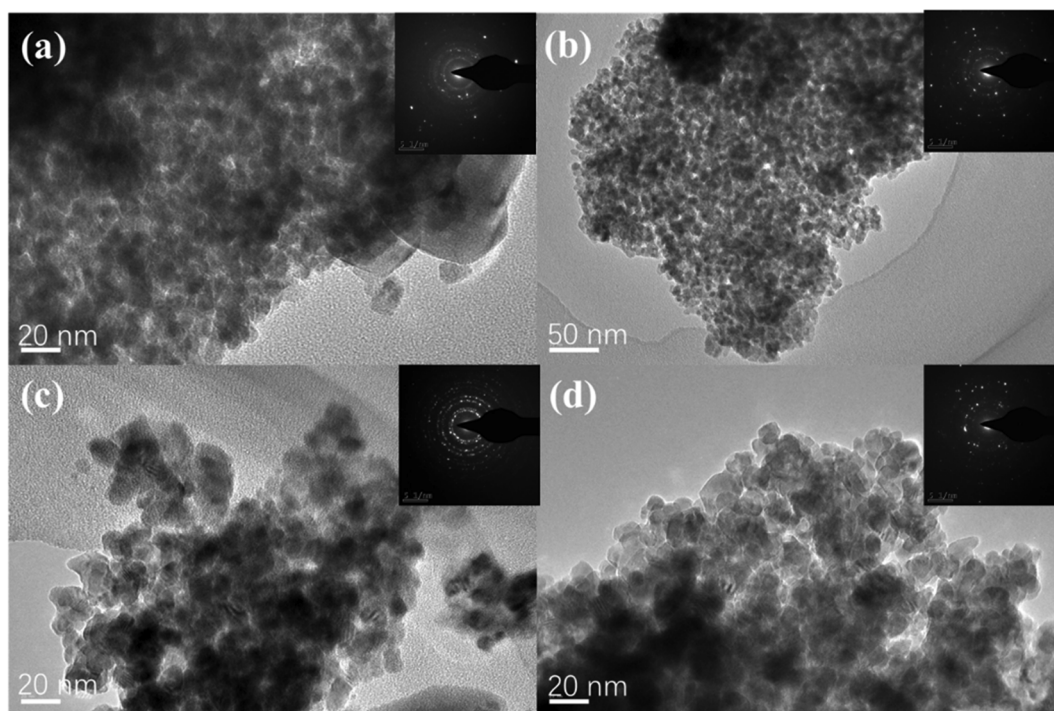


Fig. 6. Transmission electron microscope images of 15Ni/M-CexZry catalysts with different Ce/Zr ratios: (a) 15Ni/M-Ce20Zr80, (b) 15Ni/M-Ce40Zr60, (c) 15Ni/M-Ce60Zr40, (d) 15Ni/M-Ce80Zr20.



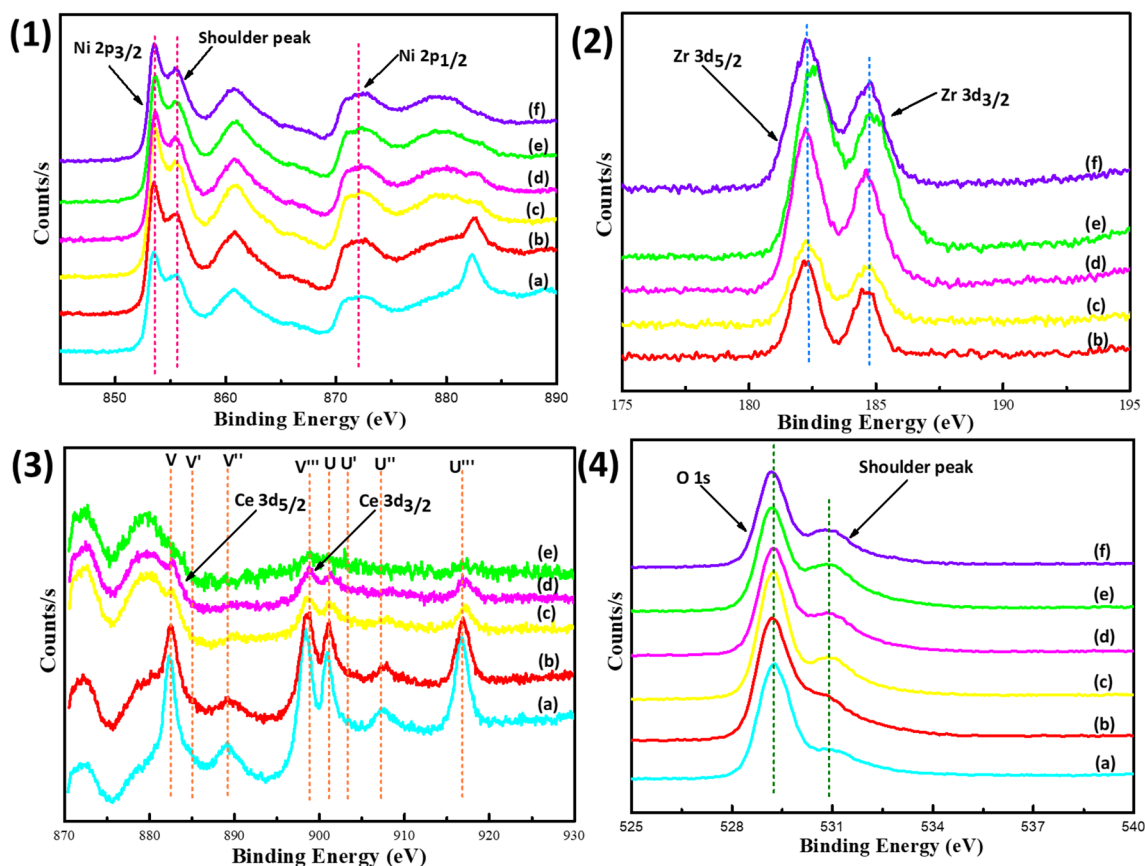


Fig. 7. X-ray photoelectron spectroscopy (XPS) of (1) Ni 2p, (2) Zr 3d, (3) Ce 3d, and (4) O 1s 15Ni/M-CexZry catalyst: (a) 15Ni/M-Ce100, (b) 15Ni/M-Ce80Zr20, (c) 15Ni/M-Ce60Zr40, (d) 15Ni/M-Ce40Zr60, (e) 15Ni/M-Ce20Zr80, (f) 15Ni/M-Zr100.

were exhibited in Fig. 9. It was found in Fig. 9 (1) that the  $H_2$ -TPR curves of all the investigated 15Ni/M-CexZry catalysts displayed reduction peaks with the similar shapes in the range of 348–598 °C, exhibiting a large reduction peak and a less pronounced shoulder peak in different temperature regions, respectively. As for the main reduction peaks in the range of 447–516 °C, they should be attributed to the reduction of the NiO species with strong interaction with the support because the pure NiO often displayed a single peak in the range of 300–400 °C [55,56]. Furthermore, it was worth noting that the positions of the main reduction peaks were different with each other because of their different Ce/Zr molar ratios, which would influence the concentration of the oxygen vacancies. Therefore, the oxygen vacancies contributed to the construction of the strong metal-support interaction. However, as regards the shoulder peaks around 540 °C, they could be ascribed to the reduction of NiO species with strong interaction with the M-CexZry support and the reduction of surface  $Ce^{4+}$  according to the previous researches [32,46]. Besides, the comparative study of the  $H_2$ -TPR of 15Ni/SiO<sub>2</sub> and 15Ni/M-Ce80Zr20 were conducted and their profiles were exhibited in Fig. 9 (2). As observed, the 15Ni/SiO<sub>2</sub> displayed two big reduction peaks around 314 °C, 476 °C and one small shoulder peak around 627 °C. As a comparison, the 15Ni/M-Ce80Zr20 only displayed the main peak at 484 °C and the shoulder peak at 551 °C. Overall, the 15Ni/M-Ce80Zr20 displayed much stronger metal-support interaction than the 15Ni/SiO<sub>2</sub> because of its much higher reduction peak temperatures. Therefore, the construction of the metal-support interaction was greatly influenced by the type of the support.

### 3.2.6. CO<sub>2</sub>-TPD analysis

The CO<sub>2</sub>-TPD profiles of 15Ni/M-CexZry and 15Ni/SiO<sub>2</sub> catalysts were shown in Fig. 10. The CO<sub>2</sub>-TPD profiles of 15Ni/M-CexZry catalysts were carefully compared and analyzed in the Fig. 10 (1).

Generally, these catalysts display similar CO<sub>2</sub>-TPD profiles in the shape. Specifically, each sample displayed a CO<sub>2</sub> desorption peak around 152 °C and another desorption peak in 284–515 °C region, which could be ascribed to the basic sites with different strength. Specifically, the desorption peak centered at 152 °C ought to originate from CO<sub>2</sub> molecules desorbed from the weak surface basic sites. It was noteworthy that the 15Ni/M-CexZry catalysts ( $x \neq 0$ ,  $y \neq 0$ ) displayed much stronger desorption peak (152 °C) intensity than the 15Ni/CeO<sub>2</sub> and 15Ni/ZrO<sub>2</sub> counterparts. This could be attributed to larger surface areas and bigger pore volumes of the Ce-Zr solid solutions, which could provide more accessible basic sites to the CO<sub>2</sub> probe molecules. Besides, the 15Ni/M-Zr100, 15Ni/M-Ce40Zr60, 15Ni/M-Ce60Zr40, and 15Ni/M-Ce80Zr20 catalysts also exhibited evident CO<sub>2</sub> desorption peaks with different intensities in the region of 284–515 °C, which were owing to the desorbed CO<sub>2</sub> molecules over the strong basic sites. Among these catalysts, the 15Ni/M-Ce80Zr20 performed the highest desorption peak intensity, which might be attributed to the strongest redox properties. In addition, 15Ni/M-Ce100 only displayed a small evident desorption peak at 252 °C owing to the structural properties of the catalyst, which displayed much smaller specific surface area than other catalysts based on the above N<sub>2</sub> physisorption analysis. This was not conducive to the chemisorption of CO<sub>2</sub> due to less exposed basic sites. Furthermore, the 15Ni/M-Zr100 also had another two weak CO<sub>2</sub> desorption peaks at 678 °C and 744 °C owing to the presence of strong basic sites. Therefore, it was concluded that the Ce/Zr ratio of the M-CexZry support greatly influenced the surface basic strength of Ce<sub>x</sub>Zr<sub>1-x</sub>O<sub>2</sub> solid solution.

Besides, the Fig. 10 (2) displayed the comparative study of the CO<sub>2</sub>-TPD profiles of 15Ni/M-Ce80Zr20 and 15Ni/SiO<sub>2</sub> catalysts. As can be observed, the 15Ni/M-Ce80Zr20 displayed two evident desorption peaks at 152 °C and 370 °C, which were assigned to the CO<sub>2</sub> molecule desorbed from the weak and strong basic sites, respectively. However,

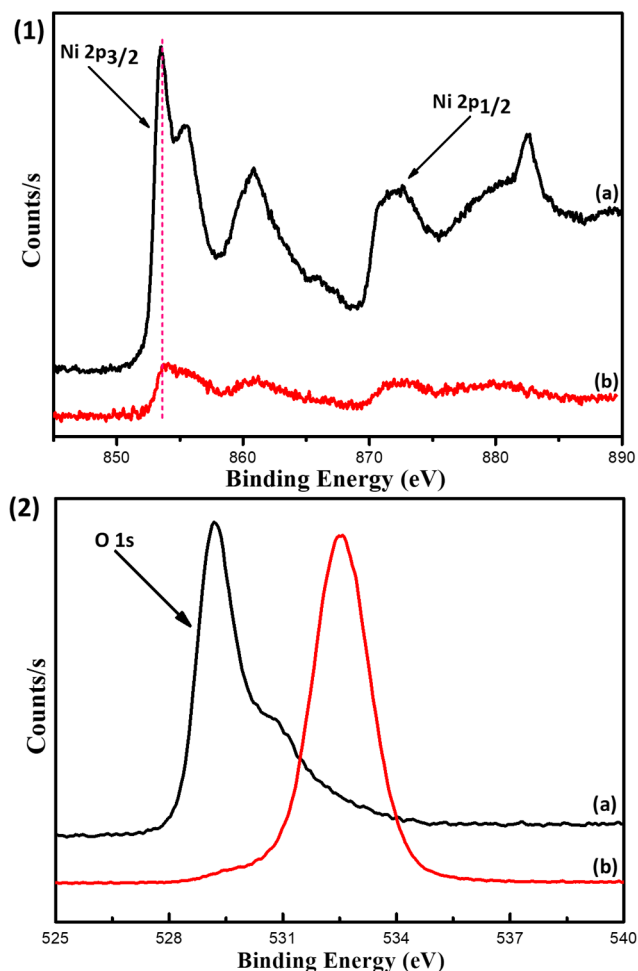


Fig. 8. X-ray photoelectron spectroscopy (XPS) of (1) Ni 2p and (2) O 1s of (a) 15Ni/M-Ce80Zr20 and (b) 15Ni/SiO<sub>2</sub> catalysts.

Table 2

Binding energy (eV) of the surface elements of the 15Ni/M-CexZry and 15Ni/SiO<sub>2</sub> catalysts.

Samples	Ni 2p <sub>3/2</sub>	O 1s	Ce 3d <sub>5/2</sub>	Zr 3d <sub>5/2</sub>
15Ni/M-Ce100	853.9	529.3	882.3	—
15Ni/M-Ce80Zr20	853.9	529.2	898.6	182.2
15Ni/M-Ce60Zr40	854.0	529.2	879.9	182.3
15Ni/M-Ce40Zr60	854.0	529.3	880.0	182.2
15Ni/M-Ce20Zr80	854.0	529.2	882.2	182.2
15Ni/M-Zr100	853.9	529.2	—	182.3
15Ni/SiO <sub>2</sub>	854.5	532.5	—	—

Table 3

O 1s peak area of the 15Ni/M-CexZry and 15Ni/SiO<sub>2</sub> catalysts.

Samples	O 1s main peak area	O 1s shoulder peak area	O 1s shoulder peak area ratio (%)
15Ni/M-Ce100	28,809	17,045	37.2%
15Ni/M-Ce80Zr20	26,541	29,016	58.0%
15Ni/M-Ce60Zr40	28,792	22,582	44.0%
15Ni/M-Ce40Zr60	23,280	24,918	51.7%
15Ni/M-Ce20Zr80	21,062	28,860	57.8%
15Ni/M-Zr100	20,732	20,534	49.8%
15Ni/SiO <sub>2</sub>	128,991	4745	3.5%

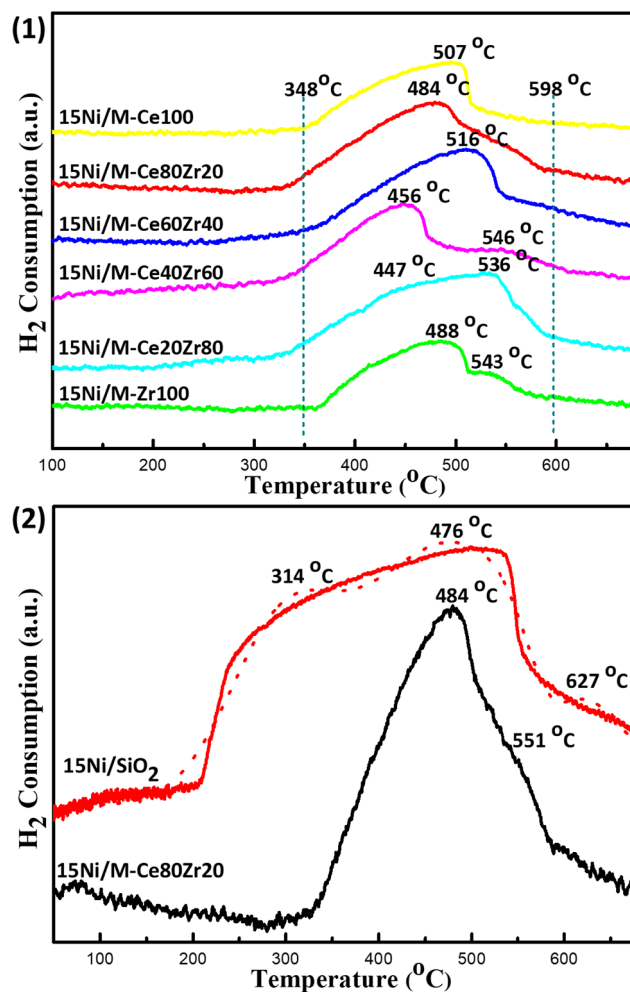


Fig. 9. (1) H<sub>2</sub> temperature-programmed reduction (H<sub>2</sub>-TPR) profiles of 15Ni/M-CexZry catalysts; (2) H<sub>2</sub>-TPR profiles of 15Ni/M-Ce80Zr20 and 15Ni/SiO<sub>2</sub> catalysts.

the 15Ni/SiO<sub>2</sub> merely performed one small evident desorption peak at 293 °C, demonstrating weak basicity over the catalyst surface. The reason for this was mainly derived from the nearly neutral SiO<sub>2</sub> surface, which was covered by the silanol (Si-OH). Furthermore, the peak intensity of the 15Ni/M-Ce80Zr20 was much higher than that over the 15Ni/SiO<sub>2</sub>. This suggested that the number of the basic site of 15Ni/M-Ce80Zr20 was also more than that of the 15Ni/SiO<sub>2</sub>. In general, the mesoporous M-Ce80Zr20 support displayed much stronger surface basicity than the commercial SiO<sub>2</sub> support.

### 3.3. Catalytic performances toward CO<sub>2</sub> methanation

#### 3.3.1. Effect of the Ce/Zr ratio on the catalytic activities

Fig. 11 displayed the results of the CO<sub>2</sub> conversion and CH<sub>4</sub> selectivity over the 15Ni/M-CexZry catalysts at different reaction temperatures. As could be observed in Fig. 11 (1), the CO<sub>2</sub> conversion gradually increased with the increase of the temperature from 200 °C to 400 °C. However, the CO<sub>2</sub> conversion suffered decline as the temperature further increased to 450 °C. It was interesting to observe that the 15Ni/M-CexZry displayed greatly different trends of CO<sub>2</sub> conversions with the chemical equilibrium CO<sub>2</sub> conversion. The reason for this was because of the confliction between the ideal thermodynamic calculation and real dynamics. For the CO<sub>2</sub> methanation, it was simultaneously controlled by both kinetic and thermodynamic influencing factors [4,6]. Although the low temperature was conducive to the achievement of the high CO<sub>2</sub> conversion, yet the methanation of CO<sub>2</sub> into CH<sub>4</sub>



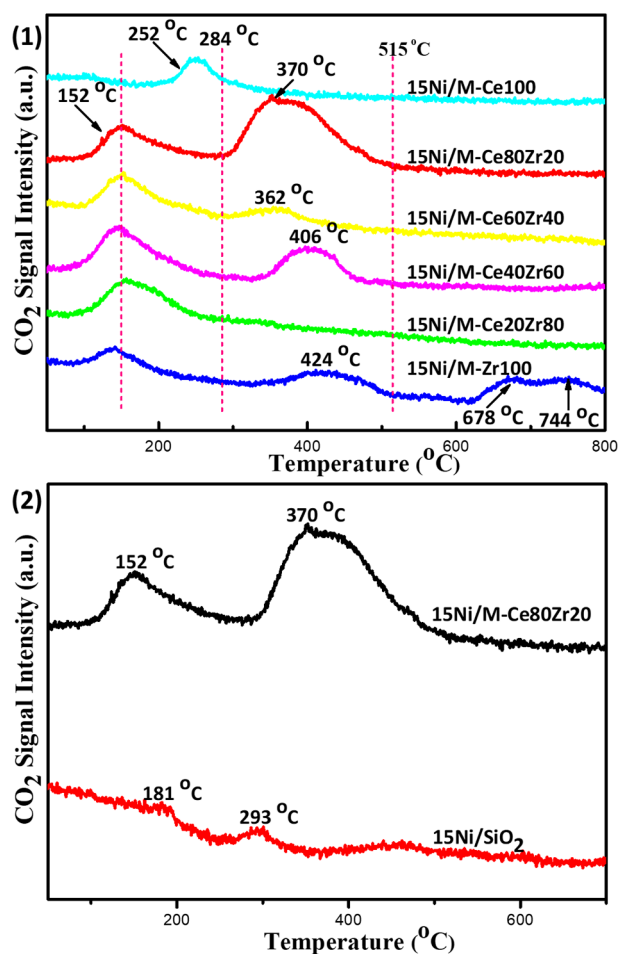


Fig. 10. (1) CO<sub>2</sub> temperature-programmed desorption (CO<sub>2</sub>-TPD) profiles of 15Ni/M-CeZr catalysts; (2) CO<sub>2</sub>-TPD profiles of 15Ni/M-Ce80Zr20 and 15Ni/SiO<sub>2</sub> catalysts.

was related to the transference of eight-electron with high kinetic barrier [4,7,16]. Thus, this process was affected by kinetics at lower temperatures and thermodynamically controlled at high temperature. In addition to this, it was noticeable that the 15Ni/M-Ce80Zr20 catalyst displayed higher low-temperature activity than other catalysts. Specifically, the CO<sub>2</sub> conversion of 15Ni/M-Ce80Zr20 (51.5%) at 280 °C was 2.60 and 4.35 times higher than those of 15Ni/M-Ce100 (19.7%) and 15Ni/M-Zr100 (11.8%) catalysts, respectively. However, the disparity between them became smaller with the increase of the reaction temperature. The reason for this could be originated from the excellent redox properties of the mesoporous Ce-Zr solid solution supports, which were greatly influenced by the Ce/Zr ratio. Therefore, the 15Ni/M-Ce80Zr20 catalyst displayed the highest activities in the range of 200–280 °C.

Fig. 11 (2) displayed the CH<sub>4</sub> selectivity of the CO<sub>2</sub> methanation over these catalysts. It was observed that the CH<sub>4</sub> selectivity of the 15Ni/M-CeZr catalysts gradually decreased with the increase of the reaction temperature. This was similar to the trend of the chemical equilibrium CH<sub>4</sub> selectivity. Generally, the decrease of the CH<sub>4</sub> selectivity at high temperature was caused by the reverse water-gas shift (RWGS) reaction [3,7,57]. Besides, it was noticeable that the 15Ni/M-CeZr catalysts displayed higher CH<sub>4</sub> selectivity than 15Ni/M-Ce100 and 15Ni/M-Zr100 catalysts with pure CeO<sub>2</sub> and ZrO<sub>2</sub> supports. The reason for this could be derived from poorer dispersion of the metallic Ni over the pure CeO<sub>2</sub> and ZrO<sub>2</sub> supports because of their low surface areas. Consequently, the dissociation of the H<sub>2</sub> over the 15Ni/M-Ce100 and 15Ni/M-Zr100 catalysts was slower than those over the 15Ni/M-

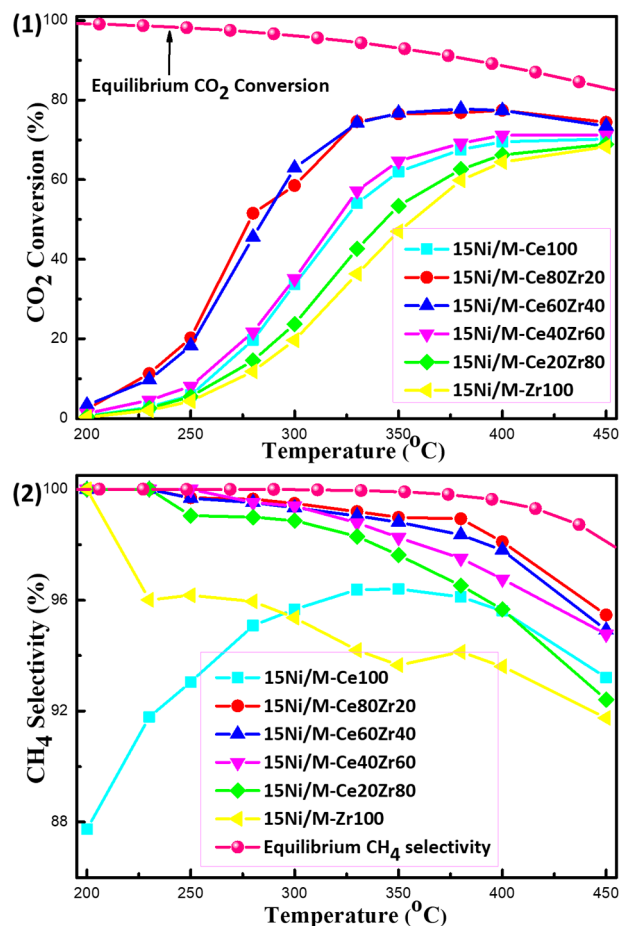


Fig. 11. (1) CO<sub>2</sub> conversion and (2) CH<sub>4</sub> selectivity over 15Ni/M-CeZr catalysts with different Ce/Zr ratios toward CO<sub>2</sub> methanation.

CeZr catalysts. Furthermore, as for the catalysts supported on mesoporous Ce-Zr solid solution, the selectivity of CH<sub>4</sub> also increased as the Ce molar percentage increased from 20% to 80%, especially at higher reaction temperature and the 15Ni/M-Ce80Zr20 was the most excellent under low temperature conditions. This implied that the Ce/Zr ratio could tune the CH<sub>4</sub> selectivity and the distribution of the products.

### 3.3.2. The effect of the redox property of the support on the catalytic activities

In order to address the role of the redox property of the support in promoting the catalytic activities, the comparison between catalytic activities of 15Ni/M-CeZr and 15Ni/SiO<sub>2</sub> catalysts were conducted at different reaction temperatures (200–450 °C). Fig. 12 displayed the results of the catalytic performances. As could be observed in Fig. 12 (1), the 15 Ni/M-Ce80Zr20 performed much higher CO<sub>2</sub> conversion than 15Ni/SiO<sub>2</sub>, especially at low temperature (< 300 °C) because it belonged to the kinetics-controlled temperature range. For example, the CO<sub>2</sub> conversion over 15Ni/M-Ce80Zr20 (51.5%) was 7.9 times higher than that over 15Ni/SiO<sub>2</sub> (6.5%) at 280 °C. However, the CO<sub>2</sub> conversions of the two catalysts were gradually close as the reaction temperature increased. This was probably attributed to the thermodynamic-controlled characteristic of the CO<sub>2</sub> methanation at high temperatures. The main reason for this could be derived from the better redox property of 15Ni/M-Ce80Zr20 than that of 15Ni/SiO<sub>2</sub> based on the XPS results in Fig. 8. The redox property of the Ce<sub>x</sub>Zr<sub>1-x</sub>O<sub>2</sub> solid solution greatly contributed to the activation of the CO<sub>2</sub> by tuning the reaction intermediates and pathway, which would be investigated by the following *in-situ* DRIFTS. Besides, the comparison of the CH<sub>4</sub>

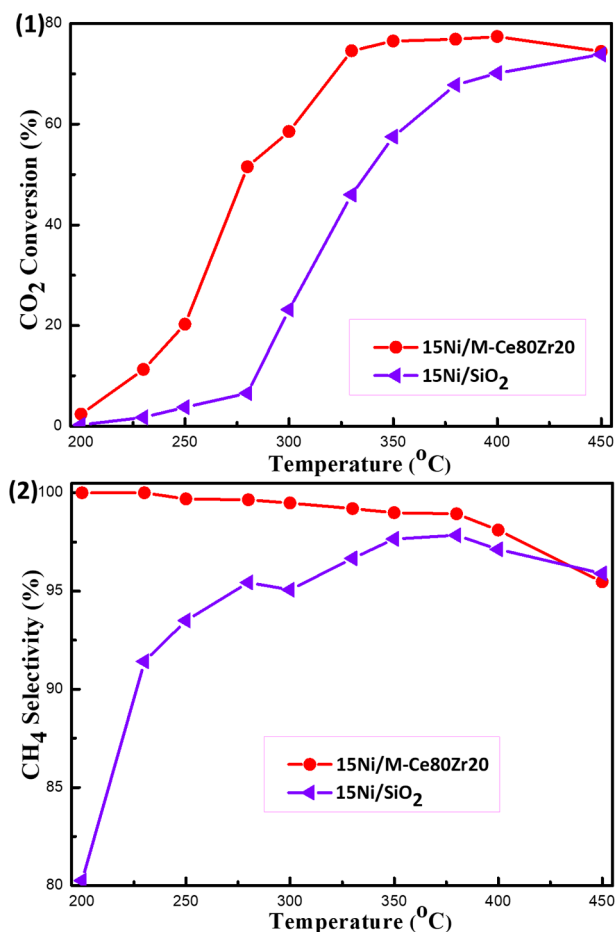


Fig. 12. (1) CO<sub>2</sub> conversion and (2) CH<sub>4</sub> selectivity over 15Ni/M-Ce80Zr20 and 15Ni/SiO<sub>2</sub> catalysts with different supports toward CO<sub>2</sub> methanation.

selectivity between 15Ni/M-Ce80Zr20 and 15Ni/SiO<sub>2</sub> was exhibited in Fig. 12 (2). As observed, 15Ni/M-Ce80Zr20 displayed much higher CH<sub>4</sub> selectivity than 15Ni/SiO<sub>2</sub>. Specifically, the CH<sub>4</sub> selectivity of 15Ni/M-Ce80Zr20 decreased slowly from 100% to 95.5% as the temperature increased, which was caused by the thermodynamic limitation. As a comparison, the CH<sub>4</sub> selectivity of 15Ni/SiO<sub>2</sub> increased from 80.2% to 95.9%. The main reason for this could be attributed to the formation of nickel carbonyl at low reaction temperature. Besides, the CH<sub>4</sub> selectivity could be also influenced by the reaction intermediates during CO<sub>2</sub> methanation, which could greatly be depended on the type of the catalytic support. Overall, compared with conventional SiO<sub>2</sub> supported reference catalyst, the 15Ni/M-CeZr catalysts performed much higher CO<sub>2</sub> conversions and CH<sub>4</sub> selectivities due to the redox property of the mesoporous Ce-Zr solid solution supports, which made great contribution to CO<sub>2</sub> activation at low temperature.

### 3.3.3. Transient study by TPSR of CO<sub>2</sub> methanation

The transient study of the TPSR of the CO<sub>2</sub> methanation over 15Ni/M-CeZr and 15Ni/SiO<sub>2</sub> catalysts were conducted to investigate the role of CO<sub>2</sub> action in methanation. The 15Ni/M-Ce100, 15Ni/M-Ce80Zr20, and 15Ni/M-Zr100 were chosen as the representatives of the 15Ni/M-CeZr catalysts. Their profiles of the trends of CO<sub>2</sub> ( $m/z = 44$ ), H<sub>2</sub> ( $m/z = 2$ ), CH<sub>4</sub> ( $m/z = 16$ ), H<sub>2</sub>O ( $m/z = 18$ ), and CO ( $m/z = 28$ ) were depicted in Fig. 13. For the TPSR profiles of these catalysts, as the temperature increased, their main trends were basically similar to each other over different catalysts. Specifically, the main trends of CO<sub>2</sub> and H<sub>2</sub> reactants were downward as the temperature increased because of the consumption of the feedstock during the CO<sub>2</sub> methanation. However, the trend of H<sub>2</sub> over most catalysts suffered

some increase when the temperature was above 400 °C. The reason for this might be attributed to the water-gas shift (WGS,  $\text{CO} + \text{H}_2\text{O} \rightarrow \text{CO}_2 + \text{H}_2$ ) side reaction, which generated the H<sub>2</sub>. As a comparison, the concentration of CH<sub>4</sub> and H<sub>2</sub>O products gradually increased as the temperature increased and achieved a maximum at different peak temperatures; further increasing the temperature caused the decrease of their concentration because of the side reaction. As well known, the rate-determining step for CO<sub>2</sub> methanation was the activation process of the CO<sub>2</sub>. Therefore, the generating temperature of CH<sub>4</sub> and maximum yield temperature of CH<sub>4</sub> on mass spectra were greatly different with each other over different catalysts. Specifically, the CH<sub>4</sub> generating and maximum yield temperatures over 15Ni/M-Ce80Zr20 (221 °C and 311 °C) were much lower than those over 15Ni/M-Ce100 (255 °C and 368 °C), 15Ni/M-Zr100 (295 °C and 404 °C), and 15Ni/SiO<sub>2</sub> (294 °C and 382 °C). This was ascribed to the outstanding redox performance of the 15Ni/M-Ce80Zr20 catalyst, which favored the CO<sub>2</sub> activation at low temperature. As for the CO, its trend monotonously increased in the investigated temperature region owing to the thermodynamic characteristics. Specifically, the amount of the CO would gradually increase with the increase of the temperature because of the RWGS side reaction, which could generate CO at high temperature. Therefore, the excellent low-temperature activity of the 15Ni/M-Ce80Zr20 catalyst had close relationship with the outstanding CO<sub>2</sub> activation ability.

### 3.3.4. In-situ DRIFTS of CO<sub>2</sub> methanation

The *in-situ* DRIFTS characterization were carried out to investigate the intermediates and possible pathways of the CO<sub>2</sub> methanation reaction over the 15Ni/M-Ce80Zr20 and 15Ni/SiO<sub>2</sub> catalysts with different supports. Their profiles were displayed in Fig. 14. Generally, the *in-situ* DRIFTS spectra of the 15Ni/M-Ce80Zr20 and 15Ni/SiO<sub>2</sub> catalysts were different in the shape in the investigated temperature range (25 °C–600 °C). Specifically, the absorbance peaks at 3740 cm<sup>-1</sup>, 3703 cm<sup>-1</sup>, 3626 cm<sup>-1</sup>, and 3600 cm<sup>-1</sup> were detected on both catalysts, which could be attributed to the hydroxyl group (–OH). However, it was interesting to find that the intensity of the hydroxyl group peak absorbance gradually decreased over 15Ni/M-Ce80Zr20 catalyst as the temperature increased, though H<sub>2</sub>O was the product of the CO<sub>2</sub> methanation. The unique surface feature of the 15Ni/M-Ce80Zr20 catalyst and a bit lower specific surface area might be the possible reasons for this phenomenon. As a comparison, the intensity of the hydroxyl group absorbance gradually increased over 15Ni/SiO<sub>2</sub> catalyst as the temperature increased. This should be originated from the dissociation of the H<sub>2</sub>O generated over the catalyst surface during the CO<sub>2</sub> methanation. Besides, the stretching vibration absorbance peak at 3015 cm<sup>-1</sup>, 2947 cm<sup>-1</sup>, and 2865 cm<sup>-1</sup> could be observed over both catalysts with different intensities, which could be derived from the C–H stretching vibration of the methylene group (=CH–), methyl group (CH<sub>3</sub>–), and –CH<sub>2</sub>– group, respectively [48,49,58]. Therefore, the CH<sub>x</sub>– (x = 1, 2, 3) species were also significant reaction intermediates during the hydrogenation process of CO<sub>2</sub> to CH<sub>4</sub> [48]. It was also worth noting that the intensity of the =CH– absorbance at 3015 cm<sup>-1</sup> gradually increased as the reaction temperature increased over the 15Ni/M-Ce80Zr20 catalyst. This suggested the fast generation of the CH<sub>4</sub> over 15Ni/M-Ce80Zr20 catalyst. In contrast, there was no big change in absorbance intensity of C–H stretching vibration over 15Ni/SiO<sub>2</sub> catalyst with the increase of the temperature. These results further confirmed that the 15Ni/M-Ce80Zr20 displayed higher catalytic activity than the 15Ni/SiO<sub>2</sub> toward CO<sub>2</sub> methanation. Besides, both catalysts displayed the infrared absorbance peaks of the gaseous CO<sub>2</sub> at 2358 cm<sup>-1</sup> and 2307 cm<sup>-1</sup> even at 25 °C [48,58]. This demonstrated that the CO<sub>2</sub> methanation reaction was started with the CO<sub>2</sub> physisorption over the catalyst surface.

As for the infrared adsorption spectra in the range of 2300–650 cm<sup>-1</sup>, they were greatly different over the 15Ni/M-Ce80Zr20 and 15Ni/SiO<sub>2</sub> catalysts because of the different features of

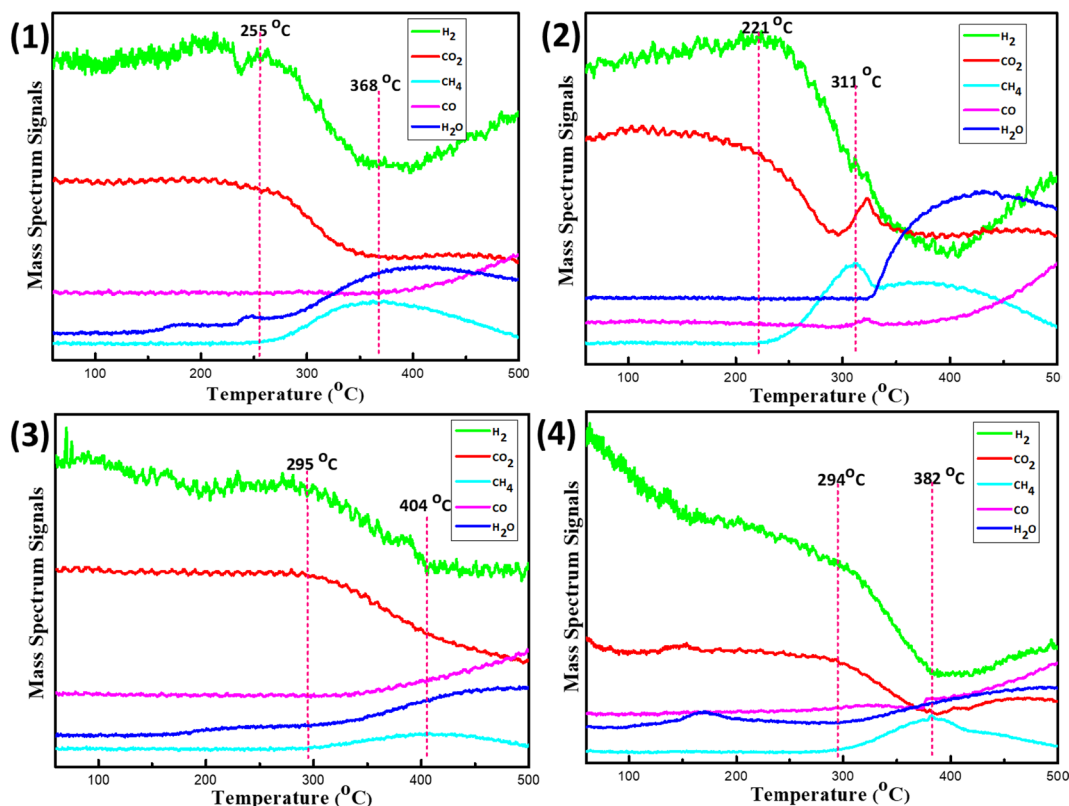


Fig. 13. Temperature-programmed surface reaction (TPSR) profiles toward  $\text{CO}_2$  methanation over different catalysts: (a) 15Ni/M-Ce100, (b) 15Ni/M-Ce80Zr20, (c) 15Ni/M-Zr100, (d) 15Ni/SiO<sub>2</sub>.

the supports. As for the 15Ni/M-Ce80Zr20 catalyst in Fig. 14 (1), it displayed monodentate formate ( $\text{HCOO}^-$ ) at  $1598\text{ cm}^{-1}$ , monodentate carbonate ( $\text{CO}_3^{2-}$ ) at  $1464\text{ cm}^{-1}$ , and bidentate formate ( $\text{HCOO}^-$ ) at  $1408\text{ cm}^{-1}$  at  $25\text{ }^\circ\text{C}$ , suggesting that the monodentate formate,

monodentate carbonate, and bidentate formate were possible reaction intermediates for the activation of the  $\text{CO}_2$  [26,59]. As the reaction temperature increased from  $25\text{ }^\circ\text{C}$  to  $600\text{ }^\circ\text{C}$ , the intensity of the monodentate formate absorbance gradually disappeared at  $200\text{ }^\circ\text{C}$  and

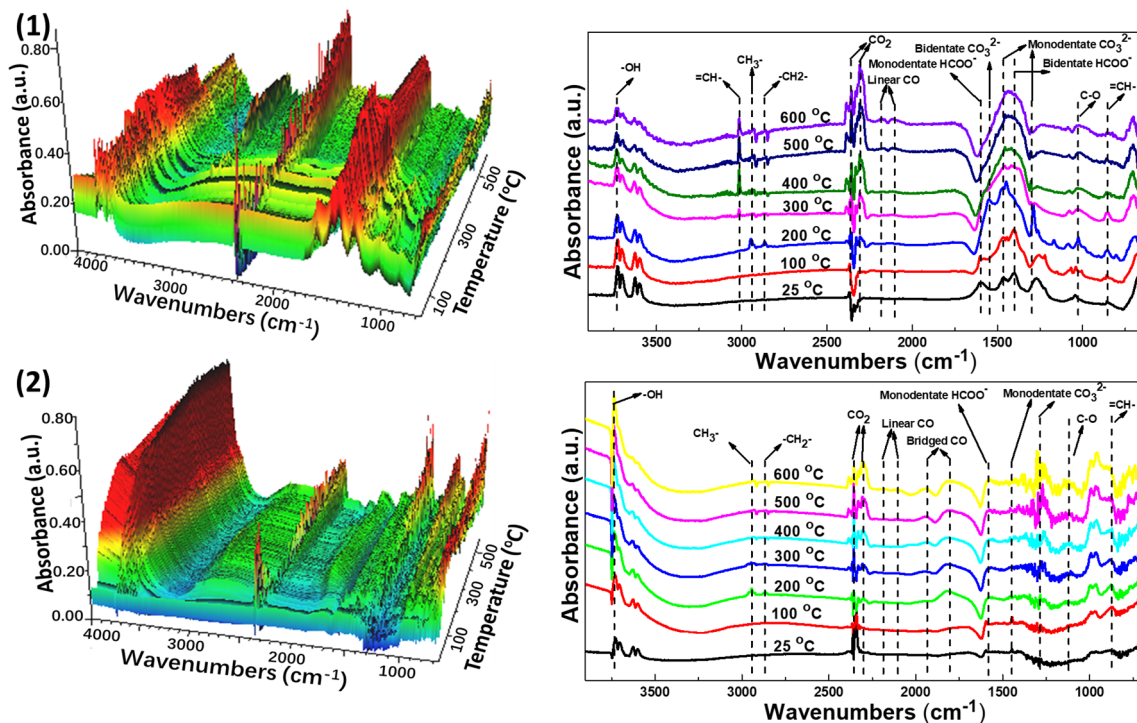


Fig. 14. The in-situ DRIFTS characterization for the methanation over the catalysts: (1) 15Ni/M-Ce80Zr20, (2) 15Ni/SiO<sub>2</sub>; reaction condition:  $\text{CO}_2/\text{H}_2 = 1/4$ ,  $\text{CO}_2 = 10\text{ mL/min}$ ,  $\text{H}_2 = 40\text{ mL/min}$ ,  $\text{N}_2 = 50\text{ mL/min}$ .



the intensities of monodentate carbonate and bidentate formate gradually increased. The infrared absorption signal of linear CO at  $2178\text{ cm}^{-1}$  and  $2116\text{ cm}^{-1}$  appeared as the temperature was above  $500\text{ }^{\circ}\text{C}$ . This could be derived from the RWGS according to the thermodynamic investigation [48]. Therefore, the monodentate carbonate and bidentate formate could be considered as the main reaction intermediates over the 15Ni/M-Ce80Zr20 catalyst. For the 15Ni/SiO<sub>2</sub> catalyst, it was found in Fig. 14 (2) that the intensities of the infrared absorption peaks of monodentate formate ( $\text{HCOO}^-$ ) at  $1598\text{ cm}^{-1}$  and bridged CO at  $1940\text{ cm}^{-1}$  and  $1810\text{ cm}^{-1}$  gradually increased with the increase of the temperature from  $25\text{ }^{\circ}\text{C}$  to  $600\text{ }^{\circ}\text{C}$  [26]. However, the intensities of the absorption peaks of monodentate carbonate ( $\text{CO}_3^{2-}$ ) at  $1446\text{ cm}^{-1}$  and  $1340\text{ cm}^{-1}$  were not greatly affected very much by the reaction temperature, especially in the range of  $25\text{--}400\text{ }^{\circ}\text{C}$  [26]. Therefore, it could be concluded that both the monodentate formate and the bridged CO are the possible reaction intermediates of the 15Ni/SiO<sub>2</sub> toward CO<sub>2</sub> methanation. The summary of the assignments of the infrared vibrational frequencies ( $\text{cm}^{-1}$ ) for possible surface reaction intermediates species was displayed in Table 4. It could be concluded that the reaction pathways over these 15Ni/M-Ce80Zr20 and 15Ni/SiO<sub>2</sub> catalysts were different. Typically, the reaction pathway over the 15Ni/M-Ce80Zr20 catalyst was the formate-route according to previous report [26]. The CO<sub>2</sub> chemisorbed over the surface of 15Ni/M-Ce80Zr20 to form the bidentate carbonates and the formates intermediates and the subsequent hydrogenation of the formates is the significant pathway for CH<sub>4</sub> synthesis. In contrast, the CO<sub>2</sub> methanation over 15Ni/SiO<sub>2</sub> took place via the CO-route. CO<sub>2</sub> chemisorbed over the 15Ni/SiO<sub>2</sub> catalyst to form monodentate carbonates and monodentate formates [26]. Then, the H atoms react with carbonates to produce monodentate formates. Then, the formates are decomposed into absorbed bridged CO. Finally, the CH<sub>4</sub> was formed by the CO hydrogenation over the Ni surface. Generally, the reaction intermediates as well as the reaction pathway over the 15Ni/M-Ce80Zr20 and 15Ni/SiO<sub>2</sub> catalysts were different owing to the different features of the catalytic supports.

### 3.3.5. Kinetic study

The kinetic studies of the 15Ni/M-CexZry and 15Ni/SiO<sub>2</sub> catalysts were conducted to investigate the roles of the Ce/Zr ratio and redox property of the catalytic support in improving the activities at low temperature. Fig. 15 showed the Arrhenius plots of the 15Ni/M-Ce100, 15Ni/M-Ce80Zr20, 15Ni/M-Zr100, and 15Ni/SiO<sub>2</sub> catalysts. It was noticeable that the slope value of the Arrhenius plot of the 15Ni/M-Ce80Zr20 catalyst was much smaller than those of the 15Ni/M-Ce100, 15Ni/M-Zr100, and 15Ni/SiO<sub>2</sub> catalysts. This suggested that the 15Ni/M-Ce80Zr20 ( $E_a = 82.9\text{ kJ/mol}$ ) performed a much lower apparent activation energy than 15Ni/M-Ce100 ( $E_a = 93.5\text{ kJ/mol}$ ), 15Ni/M-Zr100 ( $E_a = 116.4\text{ kJ/mol}$ ), and 15Ni/SiO<sub>2</sub> ( $E_a = 130.3\text{ kJ/mol}$ ) catalysts. These results demonstrated that both the Ce/Zr ratio of the 15Ni/M-CexZry catalysts and the feature of the catalytic supports could greatly influence the apparent activation energy because of different redox properties, which made great contribution to CO<sub>2</sub> activation during the process of CO<sub>2</sub> methanation.

### 3.3.6. Catalytic stability tests

The 40 h stability tests were conducted over the 15Ni/M-Ce80Zr20 and 15Ni/SiO<sub>2</sub> catalysts at  $400\text{ }^{\circ}\text{C}$  and their catalytic performances were shown in Fig. 16. As could be observed Fig. 16 (1), the CO<sub>2</sub> conversion (80.8%) of the 15Ni/M-Ce80Zr20 catalyst almost was successfully maintained after 40 h stability test. The reason for this could be attributed to the strong metal-support interaction and confinement effect of the mesopore, which could stabilize the metallic Ni active sites. As a comparison, the conversion of CO<sub>2</sub> over 15Ni/SiO<sub>2</sub> suffered from serious decline from 73.8% to 65.6%, which ought to be attributed to the serious thermal agglomeration of metallic Ni active sites. As regard the selectivity in Fig. 16 (2), the CH<sub>4</sub> selectivity of 15Ni/M-Ce80Zr20

catalyst gradually increased from 95.8% to 97.1%. In contrast, the CH<sub>4</sub> selectivity of 15Ni/SiO<sub>2</sub> catalyst decreased from 97.4% to 93.3% during the 40 h stability tests. It was reported that the CH<sub>4</sub> selectivity was traditionally sensitive to the thermal agglomeration of the metallic Ni active sites because they were responsible for dissociating H<sub>2</sub> into H [38,43]. The process of H<sub>2</sub> dissociation would be slowed down when the thermal agglomeration of the metallic Ni active sites occurred. As a result, the reaction intermediates, such as formates, carbonates, bicarbonates, etc., were more inclined to be converted into the CO because of lacking H source [38,43]. Therefore, the 15Ni/M-Ce80Zr20 mesoporous catalyst displayed more excellent catalytic stability than the 15Ni/SiO<sub>2</sub> catalyst.

## 3.4. Characterization of the 40 h spent catalysts

### 3.4.1. XRD analysis of the 40 h spent catalysts

The XRD patterns of the 40 h spent 15Ni/M-Ce80Zr20 and 15Ni/SiO<sub>2</sub> catalysts were displayed in Fig. 17. It was found that the spent 15Ni/M-Ce80Zr20 catalyst displayed obviously Ce<sub>0.8</sub>Zr<sub>0.2</sub>O<sub>2</sub> (PDF-#-28-0271) and metallic Ni (PDF-#-04-0850) characteristic diffraction peaks; as a comparison, the spent 15Ni/SiO<sub>2</sub> catalyst only displayed the characteristic metallic Ni (PDF-#-04-0850) diffraction peaks. Specifically, the peak intensity of the Ce<sub>0.8</sub>Zr<sub>0.2</sub>O<sub>2</sub> of the spent 15Ni/M-Ce80Zr20 catalyst was not so strong. This indicated that the severely thermal sintering of M-Ce80Zr20 support did not take place, demonstrating excellent stability of the support. However, the spent 15Ni/M-Ce80Zr20 catalyst displayed much weaker metallic Ni diffraction peak intensity than the spent 15Ni/SiO<sub>2</sub> catalyst. This suggested that the serious thermal agglomeration occurred over 15Ni/SiO<sub>2</sub> catalyst because of the weak metal-support interaction, accounting for the serious deactivation over the 15Ni/SiO<sub>2</sub> catalyst during the 40 h stability test. For the 15Ni/M-Ce80Zr20 mesoporous catalyst, both the confinement effect of the mesoporous support and the strong metal-support interaction greatly contributed to stabilizing the metallic Ni active sites. As a result, 15Ni/M-Ce80Zr20 mesoporous catalyst performed outstanding 40 h stability tests without obvious deactivation.

### 3.4.2. TEM analysis of the 40 h spent catalysts

Fig. 18 displayed the TEM images of the spent catalysts to investigate the morphology states of the metallic Ni nanoparticles after 40 h stability tests. As could be observed in Fig. 18 (a, b), the 40 h spent 15Ni/M-Ce80Zr20 catalyst exhibited evident mesoporous structure similar to the as-prepared 15Ni/M-Ce80Zr20 in Fig. 6 (d) and there was no large metallic Ni cluster found. This suggested that the M-Ce80Zr20 support possessed outstanding thermal stability without collapse and the agglomeration of the metallic Ni active sites during the CO<sub>2</sub>

**Table 4**

Observed infrared vibrational frequencies ( $\text{cm}^{-1}$ ) for surface reaction intermediate species on the 15Ni/M-CexZry and 15Ni/SiO<sub>2</sub> catalysts in CO<sub>2</sub> adsorption and methanation.

Surface species	Frequencies ( $\text{cm}^{-1}$ )	
	15Ni/M-Ce80Zr20	15Ni/SiO <sub>2</sub>
Monodentate carbonate ( $\text{CO}_3^{2-}$ )	1464, 1340	1464, 1340
Bidentate carbonate ( $\text{CO}_3^{2-}$ )	1550	—
Bidentate formate ( $\text{HCOO}^-$ )	1408	—
Monodentate formate ( $\text{HCOO}^-$ )	1598	1598
Bridged CO	—	1940, 1810
Linear CO	2178, 2116	2178, 2116
Methylene group ( $=\text{CH}-$ , C—H stretching vibration)	3015	—
Methyl group ( $\text{CH}_3-$ , C—H stretching vibration)	2947	2947
Methylene, ( $-\text{CH}_2-$ , C—H stretching vibration)	2865	2865



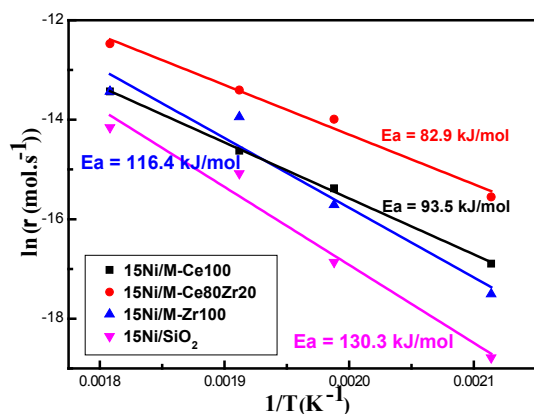


Fig. 15. Arrhenius plots for the CO<sub>2</sub> reaction rate over different catalysts with different Ce/Zr ratios and supports.

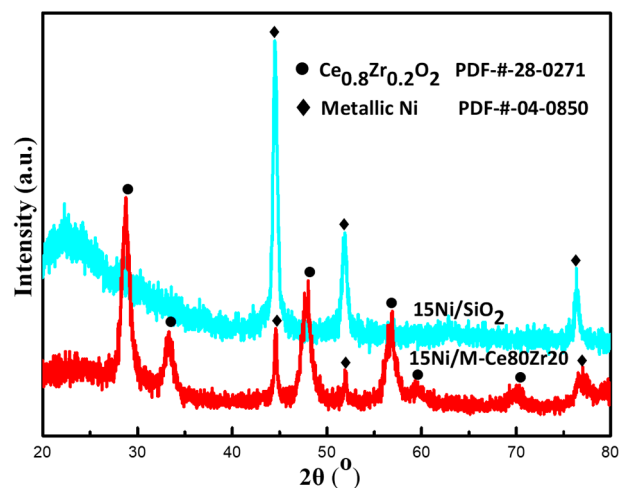


Fig. 17. XRD patterns of the spent 15Ni/M-Ce80Zr20 and 15Ni/SiO<sub>2</sub> catalysts after 40 h long-term stability tests.

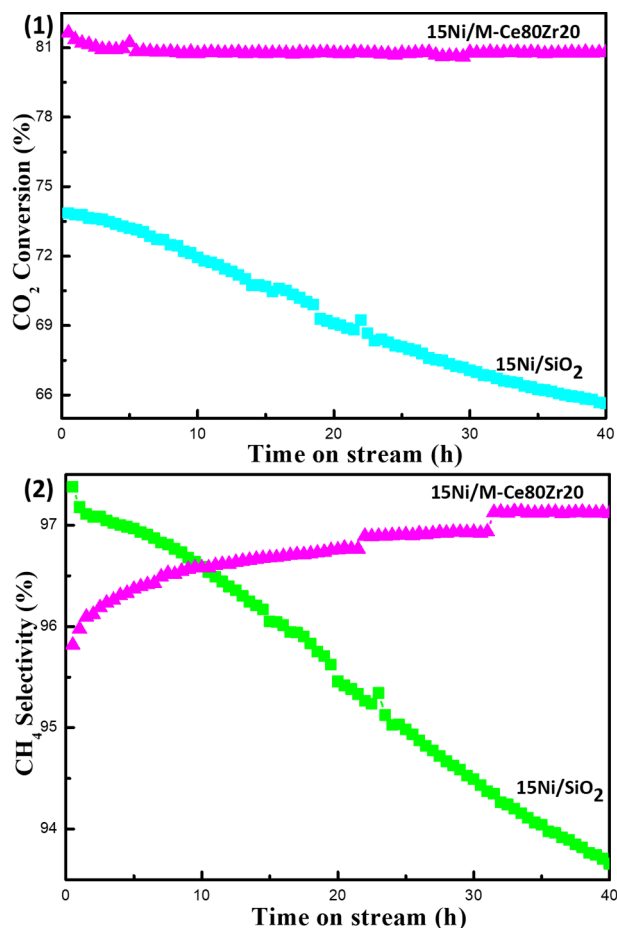


Fig. 16. 40 h long-term stability tests over 15Ni/M-Ce80Zr20 and 15Ni/SiO<sub>2</sub> catalysts: (1) CO<sub>2</sub> conversion, (2) CH<sub>4</sub> selectivity; reaction conditions: 400 °C, GHSV = 12000 mL/(g·h), H<sub>2</sub>/CO<sub>2</sub> = 4, 1 atm.

methanation were effectively inhibited. As a comparison, the spent 15Ni/SiO<sub>2</sub> catalyst displayed large metallic Ni clusters in Fig. 18 (c, d). This suggested that the serious thermal agglomeration of the metallic Ni over the 15Ni/SiO<sub>2</sub> catalyst occurred, which could be attributed to the weak metal-support interaction. Therefore, the results of the present TEM characterization of the 40 h spent catalysts were well consistent with the above XRD result in Fig. 17.

#### 4. Conclusions

In summary, a series of Ni-based catalysts supported on mesoporous Ce-Zr solid solution (Ce/Zr molar ratio = 0–100%) were prepared via the incipient impregnation method. These obtained catalysts were used as the CO<sub>2</sub> methanation catalysts. It was found that the 15Ni/M-CexZry with appropriate Ce/Zr ratio (80/20) demonstrated the best catalytic activity in low temperature region. Besides, it was also observed that the redox property of the support could greatly contribute to the improvement of the low-temperature catalytic activity. The TPSR of the CO<sub>2</sub> methanation further confirmed that the Ce/Zr molar ratio and redox property of the support could obviously influence the CO<sub>2</sub> activation at low reaction temperature. The *in-situ* DRIFTS demonstrated that the redox property of the support could greatly affect the reaction pathway of the CO<sub>2</sub> methanation by tuning the reaction intermediates. It was also found that the apparent activation energies of the catalysts were also significantly influenced by the Ce/Zr ratio and redox property of the support according to the kinetic study. Thus, the mesoporous Ce-Zr supported Ni-based catalysts preformed advanced low-temperature catalytic activity and long stability toward CO<sub>2</sub> methanation. Therefore, the Ni-based catalysts supported on the mesoporous Ce-Zr solid solutions with appropriate Ce/Zr ratio promised the potential catalysts for CO<sub>2</sub> methanation.

#### Declaration of Competing Interest

The authors declare that they have no known competing financial interests or personal relationships that could have appeared to influence the work reported in this paper.

#### Acknowledgements

The authors sincerely acknowledge the financial support from National Natural Science Foundation of China (Grant No. 21503113, 21577065, and 21976094), the National Key Research and Development Project (Grant No.2018YFC0213802), Environmental protection projects of Jiangsu province (2017022) and a Project Funded by the Priority Academic Program Development of Jiangsu Higher Education Institutions. This study was also supported by Startup Foundation of Nanjing University of Information Science and Technology.

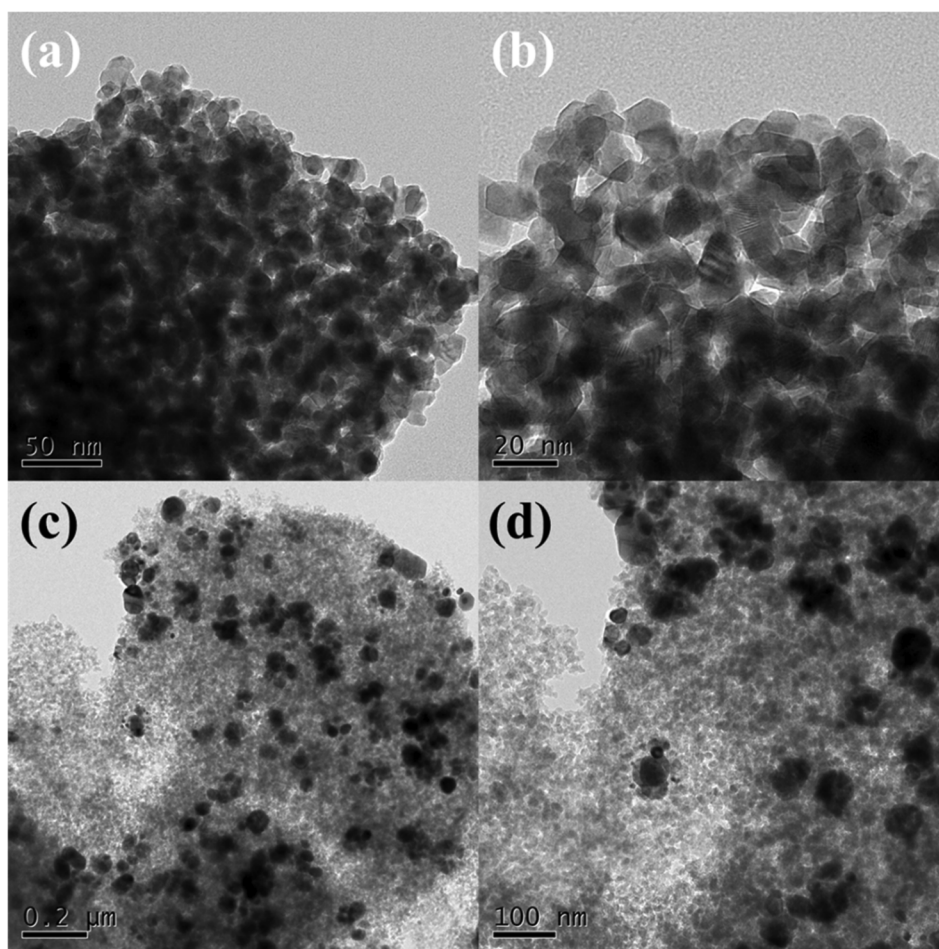


Fig. 18. Transmission electron microscope images of 40 h spent catalysts: (a) and (b) 15Ni/M-Ce80Zr20, (c) and (d) 15Ni/SiO<sub>2</sub>.

## Appendix A. Supplementary data

Supplementary data to this article can be found online at <https://doi.org/10.1016/j.fuel.2020.118813>.

## References

- [1] Asefi-Najafabady S, Rayner P, Gurney K, McRobert A, Song Y, Coltin K, et al. A multiyear, global gridded fossil fuel CO<sub>2</sub> emission data product: evaluation and analysis of results. *J Geophys Res Atmos* 2014;119. 10.213-210.231.
- [2] Peters GP, Marland G, Le Quéré C, Boden T, Canadell JG, Raupach MR. Rapid growth in CO<sub>2</sub> emissions after the 2008–2009 global financial crisis. *Nat Clim Change* 2012;2:2–4.
- [3] Stangeland K, Kalai D, Li H, Yu Z. CO<sub>2</sub> methanation: the effect of catalysts and reaction conditions. *Energy Procedia* 2017;105:2022–7.
- [4] Ghaib K, Nitz K, Ben-Fares FZ. Chemical methanation of CO<sub>2</sub>: a review. *ChemBioEng Rev* 2016;3:266–75.
- [5] Meylan FD, Moreau V, Erkman S. CO<sub>2</sub> utilization in the perspective of industrial ecology, an overview. *J CO<sub>2</sub> Util* 2015;12:101–8.
- [6] Wei W, Jinlong G. Methanation of carbon dioxide: an overview. *Front Chem Sci Eng* 2011;5:2–10.
- [7] Gao J, Liu Q, Gu F, Liu B, Zhong Z, Su F. Recent advances in methanation catalysts for the production of synthetic natural gas. *RSC Adv* 2015;5:22759–76.
- [8] Wang W, Wang S, Ma X, Gong J. Recent advances in catalytic hydrogenation of carbon dioxide. *Chem Soc Rev* 2011;40:3703–27.
- [9] Sharma S, Hu Z, Zhang P, McFarland EW, Metiu H. CO<sub>2</sub> methanation on Ru-doped ceria. *J Catal* 2011;278:297–309.
- [10] Duyar MS, Ramachandran A, Wang C, Farrauto RJ. Kinetics of CO<sub>2</sub> methanation over Ru/γ-Al<sub>2</sub>O<sub>3</sub> and implications for renewable energy storage applications. *J CO<sub>2</sub> Util* 2015;12:27–33.
- [11] Karellovic A, Ruiz P. Mechanistic study of low temperature CO<sub>2</sub> methanation over Rh/TiO<sub>2</sub> catalysts. *J Catal* 2013;301:141–53.
- [12] Beuls A, Swalus C, Jacquemin M, Heyen G, Karellovic A, Ruiz P. Methanation of CO<sub>2</sub>: Further insight into the mechanism over Rh/γ-Al<sub>2</sub>O<sub>3</sub> catalyst. *Appl Catal B: Environ* 2012;113:2–10.
- [13] Kim HY, Lee HM, Park J-N. Bifunctional mechanism of CO<sub>2</sub> methanation on Pd-MgO/SiO<sub>2</sub> catalyst: independent roles of MgO and Pd on CO<sub>2</sub> methanation. *J Phys Chem C* 2010;114:7128–31.
- [14] Karellovic A, Ruiz P. Improving the hydrogenation function of Pd/γ-Al<sub>2</sub>O<sub>3</sub> catalyst by Rh/γ-Al<sub>2</sub>O<sub>3</sub> addition in CO<sub>2</sub> methanation at low temperature. *ACS Catal* 2013;3:2799–812.
- [15] Ahmad F, Lovell EC, Masood H, Cullen PJ, Ostrikov K, Scott JA, et al. Low-temperature CO<sub>2</sub> methanation: synergistic effects in plasma-Ni hybrid catalytic system. *ACS Sustain Chem Eng* 2020.
- [16] Mebrahtu C, Krebs F, Abate S, Perathoner S, Centi G, Palkovits R. CO<sub>2</sub> methanation: principles and challenges. *Stud Surf Sci Catal*, Elsevier 2019:85–103.
- [17] Bremer J, Rätzke KH, Sundmacher K. CO<sub>2</sub> methanation: Optimal start-up control for catalytic CO<sub>2</sub> methanation reactors. *React Chem Eng* 2019;4:1019–37.
- [18] Baysal Z, Kureti S. CO<sub>2</sub> methanation on Mg-promoted Fe catalysts. *Appl Catal B: Environ* 2020;262:118300.
- [19] Aziz M, Jalil A, Triwahyono S, Ahmad A. CO<sub>2</sub> methanation over heterogeneous catalysts: recent progress and future prospects. *Green Chem* 2015;17:2647–63.
- [20] Bremer J, Rätzke KH, Sundmacher K. CO<sub>2</sub> methanation: Optimal start-up control of a fixed-bed reactor for power-to-gas applications. *AIChE J* 2017;63:23–31.
- [21] Frontera P, Macario A, Ferraro M, Antonucci P. Supported catalysts for CO<sub>2</sub> methanation: a review. *Catalysts* 2017;7:59.
- [22] Le TA, Kim MS, Lee SH, Kim TW, Park ED. CO and CO<sub>2</sub> methanation over supported Ni catalysts. *Catal Today* 2017;293:89–96.
- [23] Ye R-P, Gong W, Sun Z, Sheng Q, Shi X, Wang T, et al. Enhanced stability of Ni/SiO<sub>2</sub> catalyst for CO<sub>2</sub> methanation: Derived from nickel phyllosilicate with strong metal-support interactions. *Energy* 2019;188:116059.
- [24] Zhou R, Rui N, Fan Z, Liu C-J. Effect of the structure of Ni/TiO<sub>2</sub> catalyst on CO<sub>2</sub> methanation. *Int J Hydrogen Energy* 2016;41:22017–25.
- [25] Guilera J, del Valle J, Alarcón A, Díaz JA, Andreu T. Metal-oxide promoted Ni/Al<sub>2</sub>O<sub>3</sub> as CO<sub>2</sub> methanation micro-size catalysts. *J CO<sub>2</sub> Util* 2019;30:11–7.
- [26] Jia X, Zhang X, Rui N, Hu X, Liu C-J. Structural effect of Ni/ZrO<sub>2</sub> catalyst on CO<sub>2</sub> methanation with enhanced activity. *Appl Catal B: Environ* 2019;244:159–69.
- [27] Bian Z, Chan YM, Yu Y, Kawi S. Morphology dependence of catalytic properties of Ni/CeO<sub>2</sub> for CO<sub>2</sub> methanation: a kinetic and mechanism study. *Catal Today* 2018.
- [28] Atzori L, Cutrufello MG, Meloni D, Cannas C, Gazzoli D, Monaci R, et al. Highly active NiO-CeO<sub>2</sub> catalysts for synthetic natural gas production by CO<sub>2</sub> methanation. *Catal Today* 2018;299:183–92.
- [29] Marconi E, Tuti S, Luisetto I. Structure-Sensitivity of CO<sub>2</sub> Methanation over Nanostructured Ni Supported on CeO<sub>2</sub> Nanorods. *Catalysts* 2019;9:375.

- [30] Wang N, Qian W, Chu W, Wei F. Crystal-plane effect of nanoscale CeO<sub>2</sub> on the catalytic performance of Ni/CeO<sub>2</sub> catalysts for methane dry reforming. *Catal Sci Technol* 2016;6:3594–605.
- [31] Zhu D, Duan D, Han Y, He J, He Y, Chen Y, et al. Noble metal-free ceria-zirconia solid solutions templated by tobacco materials for catalytic oxidation of CO. *Catalysts* 2016;6:135.
- [32] Xu L, Song H, Chou L. Mesoporous nanocrystalline ceria–zirconia solid solutions supported nickel based catalysts for CO<sub>2</sub> reforming of CH<sub>4</sub>. *Int J Hydrogen Energy* 2012;37:18001–20.
- [33] Pan Q, Peng J, Sun T, Wang S, Wang S. Insight into the reaction route of CO<sub>2</sub> methanation: Promotion effect of medium basic sites. *Catal Commun* 2014;45:74–8.
- [34] Ocampo F, Louis B, Kiennemann A, Roger A. CO<sub>2</sub> methanation over Ni-Ceria-Zirconia catalysts: effect of preparation and operating conditions. *IOP Conf Ser: Mater Sci Eng*. IOP Publishing 2011:012007.
- [35] Iglesias I, Quindimil A, Mariño F, De-La-Torre U, González-Velasco JR. Zr promotion effect in CO<sub>2</sub> methanation over ceria supported nickel catalysts. *Int J Hydrogen Energy* 2019;44:1710–9.
- [36] Xu L, Wang F, Chen M, Nie D, Lian X, Lu Z, et al. CO<sub>2</sub> methanation over rare earth doped Ni based mesoporous catalysts with intensified low-temperature activity. *Int J Hydrogen Energy* 2017;42:15523–39.
- [37] Xu L, Cui Y, Chen M, Lian X, Yang B, Wu C-E, et al. Effects of the fabrication strategy on the catalytic performances of Co–Ni bimetal ordered mesoporous catalysts toward CO<sub>2</sub> methanation. *Sustainable Energy Fuels* 2019;3:3038–49.
- [38] Xu L, Wang F, Chen M, Zhang J, Yuan K, Wang L, et al. CO<sub>2</sub> methanation over a Ni based ordered mesoporous catalyst for the production of synthetic natural gas. *RSC Adv* 2016;6:28489–99.
- [39] Czuma N, Zarębska K, Motak M, Gálvez ME, Da Costa P. Ni/zeolite X derived from fly ash as catalysts for CO<sub>2</sub> methanation. *Fuel* 2020;267:117139.
- [40] Wang W, Chu W, Wang N, Yang W, Jiang C. Mesoporous nickel catalyst supported on multi-walled carbon nanotubes for carbon dioxide methanation. *Int J Hydrogen Energy* 2016;41:967–75.
- [41] Hu F, Tong S, Lu K, Chen C-M, Su F-Y, Zhou J, et al. Reduced graphene oxide supported Ni-Ce catalysts for CO<sub>2</sub> methanation: The support and ceria promotion effects. *J CO<sub>2</sub> Util* 2019;34:676–87.
- [42] Mihet M, Grad O, Blanita G, Radu T, Lazar MD. Effective encapsulation of Ni nanoparticles in metal-organic frameworks and their application for CO<sub>2</sub> methanation. *Int J Hydrogen Energy* 2019;44:13383–96.
- [43] Zhen W, Li B, Lu G, Ma J. Enhancing catalytic activity and stability for CO<sub>2</sub> methanation on Ni@ MOF-5 via control of active species dispersion. *Chem Commun* 2015;51:1728–31.
- [44] Aziz M, Jalil A, Triwahyono S, Saad M. CO<sub>2</sub> methanation over Ni-promoted mesostructured silica nanoparticles: Influence of Ni loading and water vapor on activity and response surface methodology studies. *Chem Eng J* 2015;260:757–64.
- [45] Aziz M, Jalil A, Triwahyono S, Mukti R, Taufiq-Yap Y, Sazegar M. Highly active Ni-promoted mesostructured silica nanoparticles for CO<sub>2</sub> methanation. *Appl Catal B* 2014;147:359–68.
- [46] Cui Y, Xu L, Chen M, Lian X, Wu C-E, Yang B, et al. Facilely fabricating mesoporous nanocrystalline Ce–Zr solid solution supported CuO-based catalysts with advanced low-temperature activity toward CO oxidation. *Catal Sci Technol* 2019;9:5605–25.
- [47] Cui Y, Xu L, Chen M, Lv C, Lian X, Wu C-E, et al. CO Oxidation over Metal Oxide (La<sub>2</sub>O<sub>3</sub>, Fe<sub>2</sub>O<sub>3</sub>, PrO<sub>2</sub>, Sm<sub>2</sub>O<sub>3</sub>, and MnO<sub>2</sub>) Doped CuO-Based Catalysts Supported on Mesoporous Ce<sub>0.8</sub>Zr<sub>0.2</sub>O<sub>2</sub> with Intensified Low-Temperature Activity. *Catalysts* 2019;9:724.
- [48] Liang C, Hu X, Wei T, Jia P, Zhang Z, Dong D, et al. Methanation of CO<sub>2</sub> over Ni/Al<sub>2</sub>O<sub>3</sub> modified with alkaline earth metals: Impacts of oxygen vacancies on catalytic activity. *Int J Hydrogen Energy* 2019;44:8197–213.
- [49] Zhang Z, Tian Y, Zhang L, Hu S, Xiang J, Wang Y, et al. Impacts of nickel loading on properties, catalytic behaviors of Ni/γ-Al<sub>2</sub>O<sub>3</sub> catalysts and the reaction intermediates formed in methanation of CO<sub>2</sub>. *Int J Hydrogen Energy* 2019;44:9291–306.
- [50] Hernández W, Laguna O, Centeno M, Odriozola J. Structural and catalytic properties of lanthanide (La, Eu, Gd) doped ceria. *J Solid State Chem* 2011;184:3014–20.
- [51] Peck MA, Langell MA. Comparison of nanoscaled and bulk NiO structural and environmental characteristics by XRD, XAFS, and XPS. *Chem Mater* 2012;24:4483–90.
- [52] Li W, Liu H, Chen Y. Promotion of transition metal oxides on the NH<sub>3</sub>-SCR performance of ZrO<sub>2</sub>-CeO<sub>2</sub> catalyst. *Front Environ Sci Eng* 2017;11:6.
- [53] Burroughs P, Hammett A, Orchard AF, Thornton G. Satellite structure in the X-ray photoelectron spectra of some binary and mixed oxides of lanthanum and cerium. *J Chem Soc, Dalton Trans* 1976:1686–98.
- [54] Sukonket T, Khan A, Saha B, Ibrahim H, Tantayanon S, Kumar P, et al. Influence of the catalyst preparation method, surfactant amount, and steam on CO<sub>2</sub> reforming of CH<sub>4</sub> over 5Ni/Ce<sub>0.6</sub>Zr<sub>0.4</sub>O<sub>2</sub> catalysts. *Energy Fuels* 2011;25:864–77.
- [55] Mile B, Stirling D, Zammitt MA, Lovell A, Webb M. The location of nickel oxide and nickel in silica-supported catalysts: Two forms of “NiO” and the assignment of temperature-programmed reduction profiles. *J Catal* 1988;114:217–29.
- [56] Takahashi R, Sato S, Sodesawa T, Kato M, Takenaka S, Yoshida S. Structural and catalytic properties of Ni/SiO<sub>2</sub> prepared by solution exchange of wet silica gel. *J Catal* 2001;204:259–71.
- [57] Tada S, Shimizu T, Kameyama H, Haneda T, Kikuchi R. Ni/CeO<sub>2</sub> catalysts with high CO<sub>2</sub> methanation activity and high CH<sub>4</sub> selectivity at low temperatures. *Int J Hydrogen Energy* 2012;37:5527–31.
- [58] Zhang Z, Wei T, Chen G, Li C, Dong D, Wu W, et al. Understanding correlation of the interaction between nickel and alumina with the catalytic behaviors in steam reforming and methanation. *Fuel* 2019;250:176–93.
- [59] Zhang Z, Zhang X, Zhang L, Gao J, Shao Y, Dong D, et al. Impacts of Alkali or Alkaline Earth Metals Addition on Reaction Intermediates formed in Methanation of CO<sub>2</sub> over Cobalt Catalysts. *J Energy Inst* 2020.